Journal of Molecular Graphics and Modelling 143 (2026) 109263

Contents lists available at ScienceDirect

Journal of Molecular Graphics and Modelling

journal homepage: www.elsevier.com/locate/jmgm

Quantum transport in DNA modulated by a Schiff base ligand: The role of binding and electronic structure changes from DFT–NEGF–MD simulations

Tuncay Karakurt [a,*], Alaaddin Cukurovali [b], Hashem Mohammad [c], Ibrahim Yilmaz [d,e]

[a] Department of Chemical Engineering, Faculty of Engineering–Architecture, Kırsehir Ahi Evran University, Kirsehir, 40100, Turkey
[b] Department of Chemistry, Faculty of Science, Firat University, 23119, Elazig, Turkey
[c] Department of Electrical Engineering, Kuwait University, P.O. Box 5969, Safat, 13060, Kuwait
[d] Department of Mathematics and Science Education, Faculty of Education, Bolu Abant İzzet Baysal University, 14030, Bolu, Turkey
[e] Innovative Food Technologies Development Application and Research Centre, Bolu Abant İzzet Baysal University, 14030, Bolu, Turkey

ARTICLE INFO

Keywords:
DNA charge transport
Schiff base ligand
DFT–NEGF
Molecular dynamics
HOMO–LUMO alignment
Energy–independent decoherence

ABSTRACT

DNA has emerged as a promising molecular system for nanoscale electronics owing to its self–assembly, programmability, and π–orbital delocalization. Here, we investigate the quantum charge transport behavior of a canonical 12–base–pair B–DNA duplex (RCSB ID: 102d, 5′–CGCAAATTTGCG–3′) and its Schiff-base ligand–-bound complexes. The ligand, 2–methoxy–4–((2–(4–(3–methyl–3–phenylcyclobutyl)thiazol–2–yl)hydrazono) methyl)phenol ($C_{22}H_{23}N_3O_2S$), was synthesized and structurally characterized via NMR and single–crystal X–ray diffraction. Quantum transport properties were computed using density functional theory combined with the nonequilibrium Green's function (DFT–NEGF) formalism including decoherence corrections. Transmission spectra Teff(E) and conductance G(E_F) were analyzed for bare and ligand–modified DNA systems. HOMO orbitals were found to localize strongly on the ligands, reducing conductance by ~67–76 % relative to 102d. Classical molecular dynamics and MM/GBSA binding-energy analyses were used to explore potential relationships between ligand binding strength, orbital localization, and transport suppression. Within the statistical uncertainty of the free-energy estimates, the calculations support a qualitative trend in which configurations with stronger enthalpic stabilization tend to exhibit enhanced HOMO localization and reduced conductance. However, the absence of a simple one-to-one correlation indicates that electronic transport is governed more by the specific binding mode and the resulting orbital redistribution than by the magnitude of binding affinity alone. These results therefore suggest a complex interplay between binding thermodynamics and quantum conductance, highlighting the dual role of ligand intercalation in stabilizing DNA while modulating its electronic delocalization.

1. Introduction

DNA has long been of interest in the field of molecular electronics due to its unique electronic structure, sequence diversity, and π–stacked base pairs that facilitate electron transport. As silicon–based semiconductor technologies approach physical scaling limits, biomolecules like DNA are being investigated as alternative nanoscale components for electronic devices [1–3]. Previous studies have shown that DNA conductivity is highly dependent on sequence, base pairing, environmental conditions, and conformational states (e.g., A, B, Z forms, G–quadruplexes) [4,5].

On the experimental side, single–molecule break junction (SMBJ) techniques have been widely employed to directly measure molecular conductance [6]. These measurements demonstrated that the electrical response is highly sensitive to the overall DNA conformation, enabling different structural forms to be mapped [7]. The structural properties of DNA have also been exploited to create functional devices, such as DNA nanopores that act as artificial membrane channels for bioprotonic applications [8]. Furthermore, Li et al. have shown that single–molecule conductance is sensitive enough to detect single–nucleotide polymorphisms, enabling the electrical identification of genetic material [9].

From a theoretical perspective, pioneering work by Anantram and co–workers developed unified models to explain DNA conductance by combining ab initio calculations with Green's function approaches and including decoherence effects [10,11]. The diversity of methodological approaches is also notable; for instance, some studies combine

* Corresponding author.
E-mail address: tuncay.karakurt@ahievran.edu.tr (T. Karakurt).

https://doi.org/10.1016/j.jmgm.2025.109263
Received 24 October 2025; Received in revised form 9 December 2025; Accepted 17 December 2025
Available online 22 December 2025

molecular dynamics with model Hamiltonians to assess the impact of structural fluctuations on quantum transport [12], while others focus on integrating DNA into capacitance–based [13] or other biomimetic [14] biosensor platforms. The convergence of experimental and theoretical efforts continues to deepen our understanding of these complex systems, paving the way for innovations in biophysical characterization and molecular engineering. A comprehensive picture of the interplay between DNA's structure, environment, and electronic properties is essential for understanding fundamental biophysical mechanisms and for designing next–generation molecular electronic devices (Fig. 1).

In parallel with DNA–based charge–transport studies, structurally related hydrazone and N,N–bidentate Schiff–base ligands and their metal complexes have been synthesized and characterized by combining single–crystal X–ray diffraction with DFT–based electronic structure analysis, and in some cases molecular docking toward biomolecular targets. Several reports describe isoniazid–derived Schiff bases and Cu(I) coordination complexes that were examined by SC–XRD, frontier–orbital and charge–distribution calculations, and in selected cases DNA/BSA docking and electrochemical or catalytic measurements, highlighting the close interplay between crystallographic geometry, electronic structure, and biological or functional properties [15–19]. These studies provide a complementary experimental–computational framework to the present work, in which we relate the crystallographically characterized ligand to its binding modes on DNA and to the resulting modulation of charge transport.

In the present work, we investigate the conductance properties of a canonical 12–base–pair DNA (102d, 5′–CGCAAATTTGCG–3′) and its Schiff-base (hydrazone) ligand–bound configurations (conf1, conf2, conf3, conf13). Electronic structures were obtained using DFT, and charge transport was computed via the NEGF formalism with decoherence corrections as developed by Anantram and co–workers. In addition, MD simulations were performed, and ligand binding free energies were evaluated through the g_mmpbsa approach. A key aspect of this study lies in the explicit integration of binding free energy analysis with quantum transport calculations, providing a thermodynamic framework to discuss how ligand stability may influence HOMO–level conductance suppression. By qualitatively correlating binding energetics with orbital localization and electronic transport, this work offers a unified perspective that can inform the design principles of DNA–based molecular wires.

2. Material and methods

A canonical 12–base–pair B–DNA duplex with the sequence 5′–CGCAAATTTGCG–3′ (RCSB ID: 102d) was selected as the reference system. Four configurations (conf1, conf2, conf3, and conf13) were modeled by positioning the same Schiff-base (hydrazone) ligand at different binding regions of the DNA, including intercalation and groove-binding sites. Thus, the resulting systems represent the native DNA (102d) and four ligand–bound configurations corresponding to distinct interaction modes of the same molecule. In addition, the Schiff-base ligand employed in this study was synthesized and crystallized, and its structure was characterized by single-crystal X-ray diffraction.

2.1. X–ray measurements and refinement

A suitable single crystal was selected and mounted on a Bruker AXS APEX CCD diffractometer [20] with MoK_{α} radiation for data collection. The crystal structure was solved by direct methods using the SHELXT program [21] and refined with SHELXL [22] employing full-matrix least-squares methods. Non-hydrogen atoms were refined anisotropically, except for the disordered O1A/O1B sites, which were refined isotropically with appropriate restraints to maintain chemically reasonable geometry. Hydrogen atoms bonded to carbon were positioned geometrically, with aromatic, methylene, and methyl C–H distances fixed at 0.93, 0.97, and 0.96 Å, respectively. The hydrogen atom attached to nitrogen (N2–H2) was identified using a difference Fourier map, refined isotropically, and constrained to a bond length of 0.95(2) Å. During refinement, the hydroxyl oxygen atom (O1) was found to be disordered and was modeled over two close positions, designated as O1A and O1B. The site occupancies refined to O1A = 0.60 and O1B = 0.40, with the corresponding hydrogen atoms (H1A and H1B) refined consistently to the same ratios (0.60 and 0.40, respectively). This positional disorder is attributed to the rotational flexibility of the hydroxyl group within the phenolic moiety and is a commonly observed phenomenon in related organic crystal systems. Structure visualization and refinement were conducted using Olex2 [23], while molecular graphics were prepared with the Mercury program. The crystallographic refinement parameters are summarized in Table 1 (data collection and refinement values), and the molecular arrangement is illustrated in Fig. 2.

2.2. Synthesis and crystallization

A mixture of vanillin (1.5215 g, 10 mmol) and thiosemicarbazide (0.9114 g, 10 mmol) in 30 mL of ethanol was refluxed for 2 h (TLC). Subsequently, a solution of α–haloketone (2.2271 g, 10 mmol) in 20 mL of ethanol was added dropwise at room temperature and mixture was stirred for 4 h (IR). After it was cooled to room temperature solution was poured on to crushed ice. Obtained light brown precipitate was filtered off, washed with copious water several times and dried in air and crystallized from ethanol. Yield: 67 %, melting point: 411 K. Characteristic IR bands (KBr): 3467 cm^{-1} ν(–OH), 3121 cm^{-1} ν(–NH–), 2962–2862 cm^{-1} ν(aliphatics), 1609 cm^{-1} ν(C=N thiazole), 1565 cm^{-1} ν(C=N azomethine), 1116 ν(C–O), 710 cm^{-1} ν(C–S–C thiazole). Characteristic ^{1}H NMR shifts (DMSO–d_6, δ, ppm): 1.50 (s, 3H, –CH_3), 2.38–2.43 (m, 2H, –CH_2–, in cyclobutane), 2.51–2.52 (m, 2H, –CH_2–, in cyclobutane), 3.58–3.66 (quint, j = 7.2 Hz, 1H, >CH–, in cyclobutane), 3.81 (s, 3H, –OCH_3), 6.47 (s, 1H, aromatic), 6.22 (d, j = 8.0 Hz, 1H, aromatic), 7.04–7.06 (m, 1H, aromatic), 7.16–7.21 (m, 4H, aromatics), 7.30–7.34 (m, 2H, aromatics), 7.88 (s, 1H, azomethine), 9.46 (brs, 1H, –NH–), 11.98 (brs, 1H, –OH). Characteristic ^{13}C NMR shifts (DMSO–d_6,

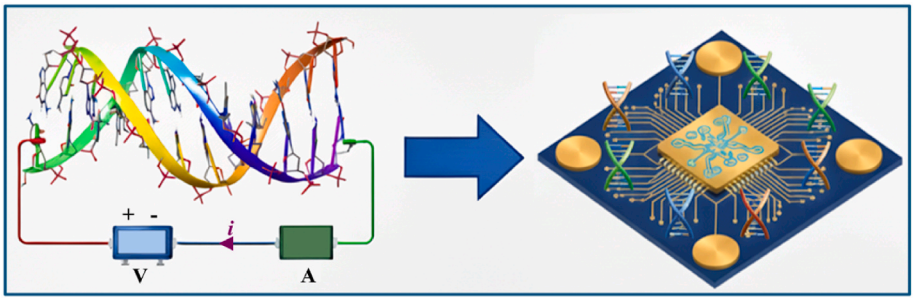

Fig. 1. Schematic illustration of the transition from single–molecule DNA conductance measurements (left) to functional DNA–based chip devices (right). The figure emphasizes the integration of molecular electronics into scalable platforms, where DNA acts as the active electronic component.

Table 1
Data collection and refinement values of the title crystal.

Empirical formula	$C_{22}H_{23}N_3O_2S$
Formula weight	393.49
Temperature/K	100
Crystal system	monoclinic
Space group	C2/c
a/Å	21.555(3)
b/Å	11.0329(14)
c/Å	19.723(2)
α/°	90
β/°	103.597(7)
γ/°	90
Volume/Å^3	4559.1(10)
Z	8
ρ_{calc}g/cm^3	1.147
μ/mm^{-1}	0.162
F(000)	1670
Crystal size/mm^3	0.3 × 0.3 × 0.2
Radiation	MoKα (λ = 0.71073)
2Θ range for data collection/°	4.47 to 56.614
Index ranges	−28 ≤ h ≤ 28, −14 ≤ k ≤ 14, −26 ≤ l ≤ 26
Reflections collected	92685
Independent reflections	5647 [Rint = 0.0495, Rsigma = 0.0250]
Data/restraints/parameters	5647/19/261
Goodness–of–fit on T2	1.021
Final R indexes [I ≥ 2σ (I)]	R1 = 0.0497, w*R*2 = 0.1185
Final R indexes [all data]	R1 = 0.0732, w*R*2 = 0.1314
Largest diff. peak/hole/e Å^{-3}	0.48/–0.46
CCDC number	**2491232**

δ, ppm): 152.68, 152.67, 148.81, 148.38, 148.37, 128.65, 128.64, 126.21, 125.71, 125.07, 120.94, 116.14, 109.84, 101.93, 56.06, 40.47, 40.24, 38.74, 30.56 see (Sch 1).

2.3. QM/MM model construction and optimization

The hybrid quantum mechanics/molecular mechanics (QM/MM) framework was employed to accurately capture the structural and electronic features of DNA–ligand complexes. The initial atomic coordinates of the canonical B–form DNA duplex (5′–CGCAAATTTGCG–3′, PDB ID: 102d) were obtained from the RCSB Protein Data Bank, and ligand intercalation geometries were generated using Discovery Studio Client based on π–π stacking alignment between aromatic rings and neighboring base pairs. For all ligand–DNA complexes, the ligand coordinates were imported directly from the experimentally determined single–crystal X–ray structure (CCDC 2491232), ensuring that the heavy–atom scaffold in the computational models matches the crystallographic conformation. In the subsequent energy minimization and QM/MM optimization steps, only hydrogen atoms and flexible peripheral torsions were allowed to relax, enabling adaptation to the DNA environment while preserving the experimentally observed ligand geometry.

All QM/MM geometry optimizations were performed using the CP2K 2025.1 package [24], which implements the *Quickstep* algorithm within the mixed Gaussian and plane–wave (GPW) formalism. The system was partitioned into two regions:

(i) the QM region, consisting of the ligand and its directly interacting nucleotides (typically two base pairs), was treated using the semi–empirical MNDO/d method, providing a balanced description of π–conjugation and hydrogen bonding; and (ii) the MM region, encompassing the remainder of the DNA duplex and the solvent, was described with the Amber force field.

The QM and MM subsystems interacted through electrostatic embedding, ensuring that the QM electronic density responded to the classical point charges of the MM environment. Nonbonded interactions between the two regions were handled via a smooth switching function, while bonded link atoms were introduced at the C–C and C–N boundary positions to preserve valence continuity across the QM/MM interface.

All classical parameters (bond, angle, dihedral, van der Waals, and partial charges) were taken from the LJ_mod.prmtop topology file generated using AmberTools. The systems were solvated with explicit TIP3P water molecules, and periodic boundary conditions were applied in all directions.

Energy minimizations were carried out until the maximum force converged below 4.5 × 10^{-4} Hartree/Bohr. The SCF convergence criterion was set to 1 × 10^{-6} Hartree, using the Orbital Transformation (OT) method with DIIS extrapolation for improved numerical stability. The electronic cutoff for the plane–wave basis was 400 Ry, and the relative cutoff was 60 Ry. Dispersion corrections were included via

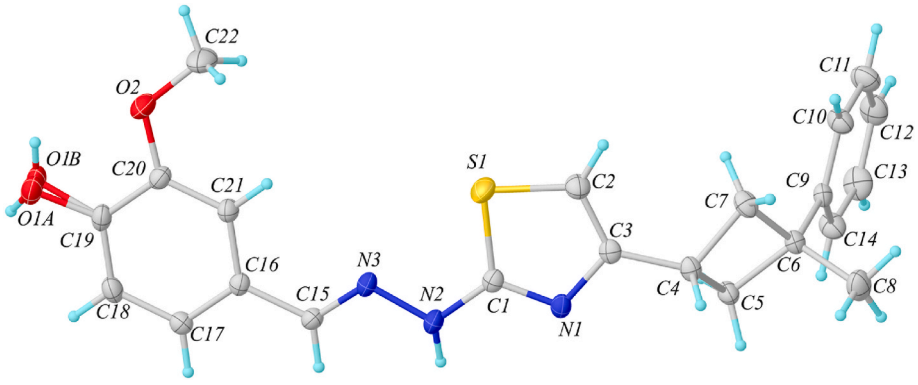

Fig. 2. Molecular structure of $C_{22}H_{23}N_3O_2S$ determined by single–crystal X–ray diffraction, showing atom labeling and coordination environment.

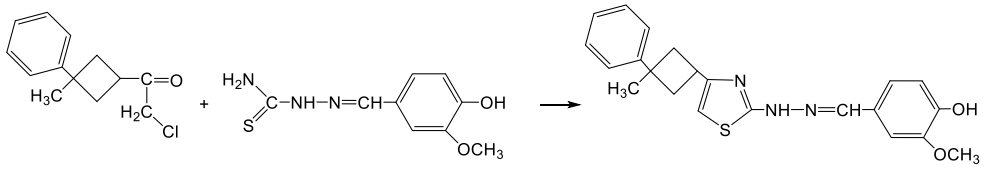

Scheme 1. Synthetic pathway for the synthesis of the target compound.

Grimme's D3 model.

During the optimization, positional restraints were gradually released from the terminal nucleotides, allowing local structural relaxation of the intercalation site. This iterative procedure yielded energetically stable ligand–DNA configurations, which were subsequently used as input geometries for electronic structure and quantum transport analyses.

2.4. Molecular dynamics simulations

All systems underwent classical molecular dynamics (MD) simulations using the GROMACS 2024.4 package [25]. The DNA duplex was described using the AMBER DNA.bsc1 force field, while the ligand was parameterized with GAFF; AM1-BCC partial charges were assigned via *antechamber* and missing parameters were obtained using *parmchk2*. The DNA–ligand complexes were assembled and processed with *pdb4amber* and built in *tleap* by sourcing the DNA.bsc1, GAFF, and TIP3P libraries and loading the ligand *prepi* and *frcmod* files. Each system was solvated with explicit TIP3P water using TIP3PBOX 8, and counterions (K^+ and Cl^-) were added to neutralize the overall charge. The resulting topologies and coordinates were saved as.prmtop and.inpcrd files for subsequent MD simulations and analyses.

Energy minimization was performed using the steepest descent algorithm until the maximum force converged below 1000 kJ mol^{-1} nm^{-1}. The minimized systems were then equilibrated in two stages: (i) an NVT ensemble for 1 ns at 300 K using the Nosé–Hoover thermostat (time constant $\tau_t = 1.0$ ps) and (ii) an NPT ensemble for 5 ns employing the Parrinello–Rahman barostat ($\tau_p = 5.0$ ps, compressibility $= 4.5 \times 10^{-5}$ bar^{-1}) to stabilize pressure at 1 bar.

Subsequently, 50 ns production MD simulations were carried out under periodic boundary conditions with a 2 fs integration timestep. The LINCS algorithm was applied to constrain all covalent bonds involving hydrogen atoms, and long–range electrostatics were treated with the Particle Mesh Ewald (PME) method (real–space cutoff = 1.2 nm). van der Waals interactions were truncated at 1.2 nm with force–switch smoothing applied between 1.0 and 1.2 nm.

Trajectory analyses were performed using GROMACS built–in utilities and in–house Python scripts to monitor RMSD, RMSF, hydrogen bonding, and ligand–DNA interaction stability over time. These analyses indicated the structural integrity of the DNA duplex and consistent ligand binding throughout the simulation.

2.5. Binding free energy calculations (MM/GBSA)

Binding free energy estimations were performed using the gmx_MMPBSA v1.6.0 tool [26] on equilibrated MD trajectories. Snapshots were extracted every 10 ps from the last 50 ns of each production run, yielding ~5000 frames per system. Each energy term was decomposed into molecular mechanics, polar solvation, nonpolar solvation, and entropic contributions. The polar solvation was estimated using the Generalized Born model (igb = 5), while the nonpolar contribution was calculated based on the solvent–accessible surface area (SASA). The entropic contribution was estimated using the interaction entropy approach.

2.6. Density functional theory and quantum transport calculations

2.6.1. Electronic structure calculations

The HOMO–LUMO orbital energies, as well as the Fock (F) and Overlap (S) matrices of all DNA and ligand–DNA systems, were obtained using Gaussian 09 [27]. Calculations were carried out at the B3LYP/6–31G(d,p) [28–30] level of theory, which has been benchmarked for nucleic acids and shown to reproduce ionization potentials and frontier orbital characteristics with reasonable accuracy [31,32], while remaining computationally efficient for large biomolecular systems (~1000 atoms). Although B3LYP is known to underestimate absolute HOMO–LUMO band gaps, the present work relies primarily on the relative alignment and spatial localization of the HOMO manifold and on qualitative trends between different binding configurations, for which this level of theory is widely regarded as adequate. Solvent effects were incorporated using the polarizable continuum model (PCM) with the integral equation formalism (IEFPCM) [33], employing a dielectric constant of $\varepsilon = 78.39$ to the represent aqueous environment. Counterions and water molecules from MD simulations were removed prior to DFT calculations to facilitate convergence. The total molecular charge was assigned following Refs. [9,11]; for the 12–base–pair duplex studied here, a total charge of −22 was used, consistent with the number of phosphodiester linkages assuming neutral terminal groups. Although this corresponds to a highly charged anionic system, the DFT calculations are not performed in the gas phase but in an aqueous polarizable continuum, so that the backbone charge is strongly screened and the electrostatic environment effectively mimics the presence of counterions and solvent. This treatment may over–stabilize the occupied manifold on an absolute energy scale; however, all bare and ligand–bound systems considered here carry the same nominal charge and are described with the same dielectric model. As a result, systematic shifts in orbital energies are expected to largely cancel when comparing different configurations, and our analysis focuses on relative changes in frontier–orbital alignment and spatial localization upon ligand binding, which are much less sensitive to this approximation.

Single–point energy calculations were performed to obtain the Fock and overlap matrices, which were subsequently transformed into an orthogonal basis using the Löwdin transformation [34]:

$$H_0 = S^{-1/2} F S^{-1/2} \tag{1}$$

where H_0 represents the Hamiltonian in the orthogonal atomic orbital basis.

2.6.2. Hamiltonian partitioning and orbital analysis

To facilitate transport calculations, the DNA Hamiltonian was partitioned into nucleotide blocks (base + backbone) [10,35]. Each nucleotide block m was diagonalized independently through a unitary transformation:

$$H = U^{\dagger} H_0 U \tag{2}$$

where U is a block–diagonal matrix composed of eigenvectors of each nucleotide sub–Hamiltonian. This transformation yields a Hamiltonian where diagonal blocks contain molecular orbital energies of individual nucleotides, while off–diagonal blocks represent inter–nucleotide hopping parameters [36].

The resulting Hamiltonian in second quantization is:

$$H = H_D + H_{OD} = \sum_{k,m} \epsilon_{k,m} c^{\dagger}_{k,m} c_{k,m} + \sum_{k,m \neq k',m'} t_{k,m \to k',m'} \left(c^{\dagger}_{k,m} c_{k',m'} + H.c \right) \tag{3}$$

where $\epsilon_{k,m}$ is the k–th molecular orbital energy of nucleotide m, $t_{k,m \to k',m'}$ represents electronic coupling between orbitals, and $c^{\dagger}$, c are creation and annihilation operators, respectively. The term *H.c is the Hermitian conjugate* denotes the Hermitian conjugate, ensuring that the Hamiltonian is Hermitian ($H = H^{\dagger}$) [4].

2.6.3. Non–equilibrium Green's function (NEGF) formalism

Charge transport through DNA was modeled using the NEGF method [37,38] with Büttiker probes [39,40] to incorporate decoherence effects arising from environmental interactions, structural fluctuations, and electron–phonon coupling. The retarded Green's function is obtained by solving [4,9]:

$$[ES - H - \Sigma_L(E) - \Sigma_R(E) - \Sigma_B(E)] G^r(E) = I \tag{4}$$

where E is energy, S is the overlap matrix, H is the partitioned Hamiltonian from equation (2), and $\Sigma_{L(R)}$ are the left (right) electrode

self–energies. Σ_B represents the decoherence self–energy arising from Büttiker probes. The advanced Green's function is obtained as [11]:

$$G^a(E) = [G^r(E)]^\dagger \tag{5}$$

2.6.4. Contact Self–Energies

Gold electrodes were modeled using the wide–band limit (WBL) approximation [41], valid when the density of states in the metal is approximately constant near the Fermi level. The contact self–energies are:

$$\Sigma_{L(R)} = -i\frac{\Gamma_{L(R)}}{2}\delta_{kk'}\delta_{mm'} \tag{6}$$

where $\Gamma_{L(R)} = 100$–600 meV represents the coupling strength between DNA and electrodes, applied to molecular orbitals at the 3′ and 5′ terminal guanine bases [9,11]. The corresponding broadening functions are:

$$\Gamma_{L(R)}(E) = i\left[\Sigma_{L(R)}(E) - \Sigma^\dagger_{L(R)}(E)\right] = \Gamma_{L(R)} \tag{7}$$

which is energy–independent within the WBL approximation [41].

2.6.5. Decoherence model

In this work we employ an energy-independent Büttiker-probe decoherence model, in which the environmental self-energy takes the form [4]:

$$\mathrm{Im}[\Sigma_B]_{kk',mm'} = -\frac{\Gamma_B}{2}\delta_{kk'}\delta_{mm'} \tag{8}$$

Here, k (k') represent the k–th (k'–th) molecular orbital energy of nucleotide m (m'). Γ_B is a constant phenomenological broadening parameter which determines the maximum decoherence strength (typically 100 meV for DNA in aqueous solution, consistent with estimates for solvated aromatic molecules [42,43]). This approach has been widely used in charge-transport studies of molecular systems and provides a straightforward means of incorporating environmentally induced phase-breaking and lifetime effects within the non-equilibrium Green's-function formalism. Because Γ_B is energy-independent, the real part of the corresponding self-energy vanishes, $\mathrm{Re}[\Sigma_B] = 0$.

Although energy-independent decoherence schemes have been developed to more precisely localize dephasing near molecular resonances and to preserve the global density of states across the full spectrum, energy-independent models have been shown to reliably capture qualitative transport behavior—particularly near the HOMO band edge and across the bandgap provided that Γ_B is chosen within a physically reasonable range [4]. This yields physically consistent trends in the relative conductance of different sequences within our energy window of interest, while maintaining methodological simplicity and reducing parameter sensitivity.

Büttiker probes were applied to all molecular orbitals except those at the contact sites (terminal nucleotides) [39,40]. For a system with N nucleotides, $N_B = N - 2$ decoherence probes were deployed. The zero–current condition at each Büttiker probe m enforces:

$$I_m = \frac{2e}{h}\sum_{n=1}^{N} T_{mn}(E)[\mu_m - \mu_n] = 0, m = 1, 2, \ldots, N_B \tag{9}$$

where $T_{mn}(E)$ is the transmission probability between probes m and n, and μ_m is the electrochemical potential at probe m [39]. The transmission probability is calculated as:

$$T_{mn}(E) = \mathrm{Tr}\left[\Gamma_m(E)G^r_{m,n}(E)\Gamma_n(E)G^a_{n,m}(E)\right] \tag{10}$$

where $\Gamma_m(E) = 2\mathrm{Im}[\Sigma_B(E)]_{mm}$ is the coupling to the m–th Büttiker probe, and $G^r_{m,n}$ are the retarded Green's function matrix elements connecting regions m and n.

Solving equation (9) for all Büttiker probes yields [39]:

$$\mu_m - \mu_L = \left(\sum_{j=1}^{N_B} W^{-1}_{mj}T_{jR}\right)(\mu_R - \mu_L), m = 1, 2, \ldots, N_B \tag{11}$$

where the matrix W_{mj} is the inverse of the matrix W_{ij} defined as:

$$W_{ij}(E) = (1 - R_{ii})\delta_{ij} - T_{ij}(1 - \delta_{ij}) \tag{12}$$

with $R_{ii} = 1 - \sum_{j\neq i}T_{ij}$ being the reflection probability at probe i.

2.6.6. Transmission and conductance

The effective transmission through the DNA junction is calculated as [10,39]:

$$T_{\mathrm{eff}}(E) = T_{LR}(E) + \sum_{i,j=1}^{N_B} T_{Li}(E)W^{-1}_{ij}(E)T_{jR}(E) \tag{13}$$

where T_{LR} is the coherent tunneling contribution (direct transmission from left to right electrode), and the second term accounts for sequential hopping via decoherence probes (incoherent transport).

The current through the left electrode is given by Ref. [37]:

$$I_L = \frac{2e}{h}\int_{-\infty}^{+\infty} T_{\mathrm{eff}}(E)\left[f_L(E) - f_R(E)\right]dE \tag{14}$$

where $f_{L(R)}(E)$ are the Fermi–Dirac distributions at the left and right electrodes:

$$f_{L(R)}(E) = \frac{1}{1 + \exp\left[\left(E - E_{F,L(R)}\right)/k_BT\right]} \tag{15}$$

with $E_{F,L(R)}$ being the Fermi energies of the electrodes.

In the linear response regime (low bias voltage V), the conductance is obtained from the Landauer–Büttiker formula [37,38]:

$$G(E_F, T) = \lim_{V\to 0}\frac{I_L}{V} = \frac{2e^2}{h}\int_{-\infty}^{+\infty} T_{\mathrm{eff}}\left(E\right)\left(-\frac{\partial f(E - E_F)}{\partial E}\right)dE \tag{16}$$

where $G_0 = 2e^2/h \approx 7.75 \times 10^{-5}\Omega^{-1}$ is the quantum of conductance, E_F is the equilibrium Fermi energy, and the derivative of the Fermi function is:

$$-\frac{\partial f(E - E_F)}{\partial E} = \frac{1}{4k_BT}\mathrm{sech}^2\left(\frac{E - E_F}{2k_BT}\right) \tag{17}$$

At room temperature ($T = 300$ K), $k_BT = 25.9$ meV. At zero temperature, the conductance simplifies to Ref. [37]:

$$G(E_F, T = 0) = G_0 \cdot T_{\mathrm{eff}}(E_F) \tag{18}$$

For finite temperature calculations, numerical integration of equation (16) was performed using adaptive quadrature with energy mesh spacing of 1–10 meV depending on the spectral features.

2.6.7. Density of states

Local and total density of states (DOS) were computed from the Green's function as [11,44]:

$$\mathrm{DOS}(E) = -\frac{1}{\pi}\mathrm{Im}\{\mathrm{Tr}[G^r(E)]\} \tag{19}$$

For site–projected DOS at nucleotide m:

$$\mathrm{DOS}_m(E) = -\frac{1}{\pi}\mathrm{Im}\left\{\mathrm{Tr}\left[G^r_{mm}(E)\right]\right\} \tag{20}$$

For orbital–resolved DOS of the k–th molecular orbital at nucleotide m:

$$\mathrm{DOS}_{k,m}(E) = -\frac{1}{\pi}\mathrm{Im}\left\{G^r_{k,m;k,m}(E)\right\} \tag{21}$$

This analysis enabled identification of HOMO localization and contributions from intercalators to the electronic structure [9,11]. Two–dimensional DOS maps were constructed as DOS(E, m) to visualize energy level distributions along the DNA strand.

The rate of Fermi energy shift due to partial charge transfer (δn) upon contact formation was estimated from Ref. [44]:

$$\frac{dE_F}{dn} = \left[\frac{dn(E_i)}{dE_i}\right]^{-1} \tag{22}$$

where the electron number as a function of energy is:

$$n(E_i) = \int_{-\infty}^{E_i} \mathrm{DOS}(E)dE = \int_{-\infty}^{+\infty} \mathrm{DOS}(E)f(E-E_i)dE \tag{23}$$

This quantity provides insight into how molecular orbital energies shift upon contact formation, which is crucial for understanding length–dependent conductance trends and the position of the Fermi level relative to HOMO [9,41].

3. Results and discussion

3.1. Binding configurations of Ligand–DNA complexes

Four distinct DNA–ligand binding configurations (conf1, conf2, conf3, and conf13) were constructed based on the canonical 12–base–pair DNA duplex. Ligands were positioned near specific base–pair regions to explore different intercalation modes, and their geometries were subsequently optimized using a QM/MM approach. Following relaxation, each system converged to a stable configuration characterized by π–π stacking between the ligand and the neighboring base pairs.

The optimized binding arrangements were as follows: conf1 (terminal intercalation at base pairs 1–24/2–23), conf2 (intercalation at base pairs 6–19/7–18), conf3 (intercalation near base pairs 11–14/12–13), and conf13 (dual binding with one ligand intercalated at the terminal base pairs 1–24/2–23, as in conf1, and a second ligand intercalated near base pairs 11–14/12–13, as in conf3). These distinct configurations were used as the initial geometries for subsequent electronic–structure and quantum–transport calculations (Fig. 3).

Following the structural analysis of ligand–DNA binding configurations, the electronic properties were evaluated in terms of the HOMO level (Fig. 4).

In the bare DNA (102d), the HOMO orbitals were found to be delocalized along the base pairs. In contrast, in all ligand–bound systems, the HOMO orbitals became strongly localized on the ligands. For the conf1 system (ligand bound at the terminal base pairs 1–24/2–23), the HOMO was calculated at −4.49 eV, the LUMO at −1.82 eV, yielding a bandgap of 2.67 eV, with the HOMO density concentrated on the ligand (Fig. 5). In conf2 (ligand intercalated at base pairs 6–19/7–18), the HOMO was −4.34 eV, the LUMO –1.82 eV, and the bandgap 2.52 eV, with the HOMO localization shifted toward the intercalation site. In conf3 (ligand intercalated near base pairs 11–14/12–13), the HOMO was −4.73 eV, the LUMO –1.85 eV, and the bandgap 2.88 eV, where the central binding caused the HOMO to localize strongly on the ligand. Finally, in the dual–ligand conf13 system (ligands bound at 1–24/2–23 and 11–14/12–13), the HOMO was −4.45 eV, the LUMO –1.84 eV, and the bandgap 2.60 eV, with both ligands completely disrupting the HOMO delocalization along DNA and confining the orbital density to the ligand regions.

These results demonstrate that ligand binding perturbs the intrinsic electronic structure of DNA, suppresses HOMO orbital delocalization, and restricts the electronic transport pathway compared to the bare 102d duplex. Similar trends have been reported in previous studies, where intercalating ligands disrupted π–stacking interactions and led to orbital localization on the ligand moieties, thereby reducing charge delocalization along the DNA backbone [5]. In addition, comparative transport analyses on ligand–DNA complexes confirm that the HOMO orbitals are predominantly shifted toward the intercalators, which results in diminished conductance relative to the bare DNA sequences [11].

3.2. Decoherent transmission spectra of DNA and Ligand–DNA

Decoherent transport calculations provide critical insights into how environmental scattering and phase-breaking effects modify charge transport in DNA. The computed Transmission spectra (Fig. 6) reveal pronounced differences between the bare DNA (102d) and ligand–-bound systems (conf1, conf2, conf3, conf13). In the bare DNA, the average log T value is around −3.9, showing relatively regular but low–amplitude resonances across the studied energy range. This behavior is consistent with previously reported results [3,5], where preserved π–stacking interactions allow frontier orbitals to remain delocalized along the DNA backbone, supporting coherent transport channels.

In the ligand–bound systems, however, the situation is notably altered. In conf1 (terminal binding at base pairs 1–24/2–23), the average log T increases to −3.50 compared to the bare DNA, indicating slightly enhanced transmission. This enhancement, however, does not originate from delocalized conduction along the helix but rather from short–range contributions localized on the ligand orbitals. In conf2

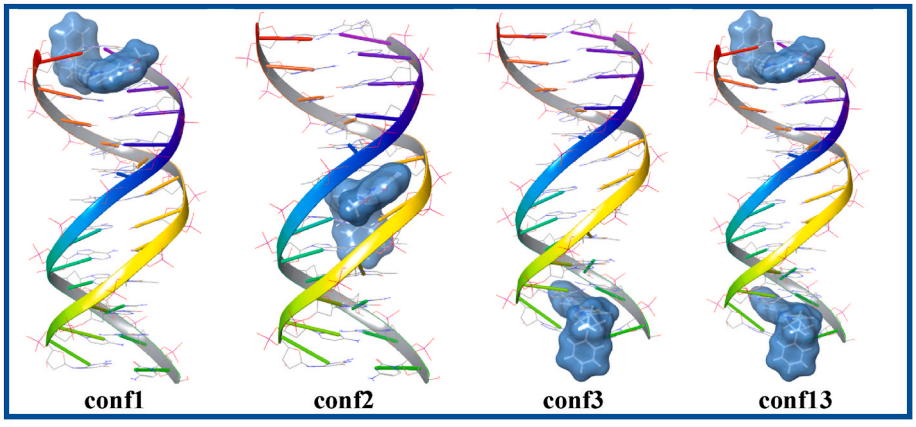

Fig. 3. Representative binding conformations of ligands in DNA duplex (sequence 5′–CGCAAATTTGCG–3′, PDB ID: 102d). Four ligand–bound systems are shown: conf1 (terminal binding at base pairs 1–24/2–23), conf2 (intercalation at base pairs 6–19/7–18), conf3 (intercalation near base pairs 11–14/12–13), and conf13 (dual binding at both DNA termini, with ligands located at base pairs 1–24/2–23 and 11–14/12–13). Ligands are displayed in surface representation (blue), and the DNA backbone in ribbon form. *For clarity, water molecules and ions are omitted from the figure.*

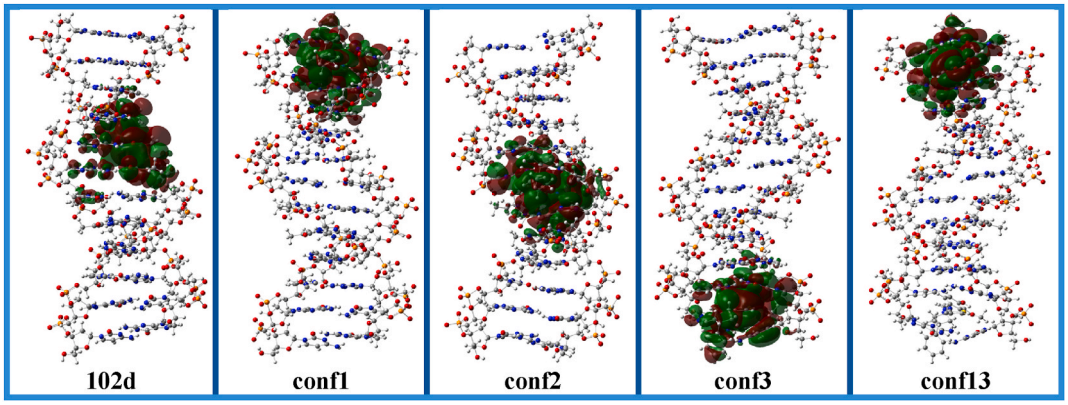

Fig. 4. HOMO orbital distributions. Spatial localization of the HOMO orbitals for the bare DNA (102d) and four ligand–bound systems (conf1, conf2, conf3, conf13). While the HOMO density is delocalized along the base pairs in the bare 102d duplex, in all ligand–bound systems the orbitals are largely confined to the ligand regions. Notably, in the dual–ligand system (conf13), the orbital is exclusively localized on the top ligand (L1–L2 region), indicating a charge trap state and lack of coupling between the two ligands.

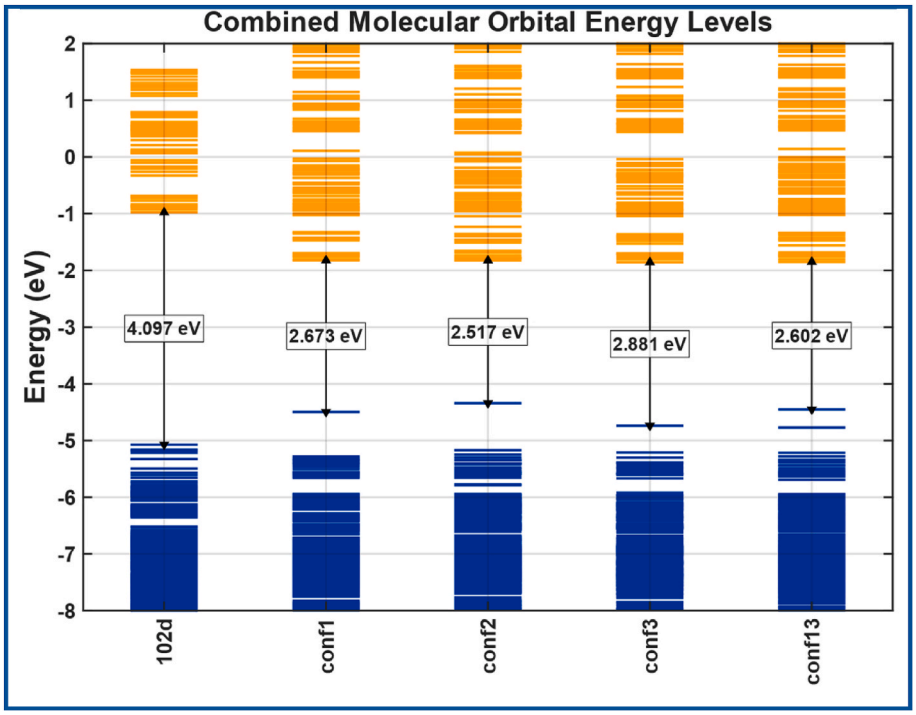

Fig. 5. Combined molecular orbital energy levels (occupied, blue; unoccupied, orange) for the bare DNA duplex (102d) and the four ligand–bound systems (conf1, conf2, conf3, conf13).

(intercalation at base pairs 6–19/7–18) and conf3 (intercalation near base pairs 11–14/12–13), the maximum log T values reach −1.67 and −1.62, respectively, much higher than those of the bare DNA. This indicates that HOMO orbitals become strongly localized on the intercalated ligands, forming new transport channels at the binding sites. Similar trends have been reported in the literature [5,11], where ligand intercalation perturbs the electronic structure of DNA and favors localized transport pathways.

Charge transport in DNA is, however, widely understood to be dominated by **hole conduction**, with the electrode Fermi level positioned close to the HOMO edge of the π–stack of nucleobases [45]. Consequently, what matters for the low–bias conductance is the value of the transmission function at the Fermi level, Teff(E_F), rather than the absolute height of off–resonant peaks. In the ligand–bound systems, most of the ligand–induced resonances are narrow, localized, and slightly shifted away from E_F, so their contribution to Teff(E_F) is negligible. In contrast, the bare 102d duplex, although characterized by lower transmission maxima, retains broader and more delocalized channels around E_F, which are far more efficient in sustaining charge transport.

In conf13 (dual binding at both termini, base pairs 1–24/2–23 and 11–14/12–13), the average log T reaches −3.41, the highest among all systems. However, this does not imply an improvement of the DNA transport capacity. Instead, the dual occupation effectively disrupts the delocalized transport mechanism of the DNA backbone, confining conduction almost exclusively to the ligand regions. Such a disruption of π–stacking and suppression of delocalized conduction has also been emphasized in previous reports [5,11].

In summary, the decoherent transmission spectra confirm that ligand binding alters the intrinsic transport mechanism of DNA by localizing HOMO orbitals on the ligands, suppressing delocalized conduction pathways, and redistributing charge transport in a manner distinct from

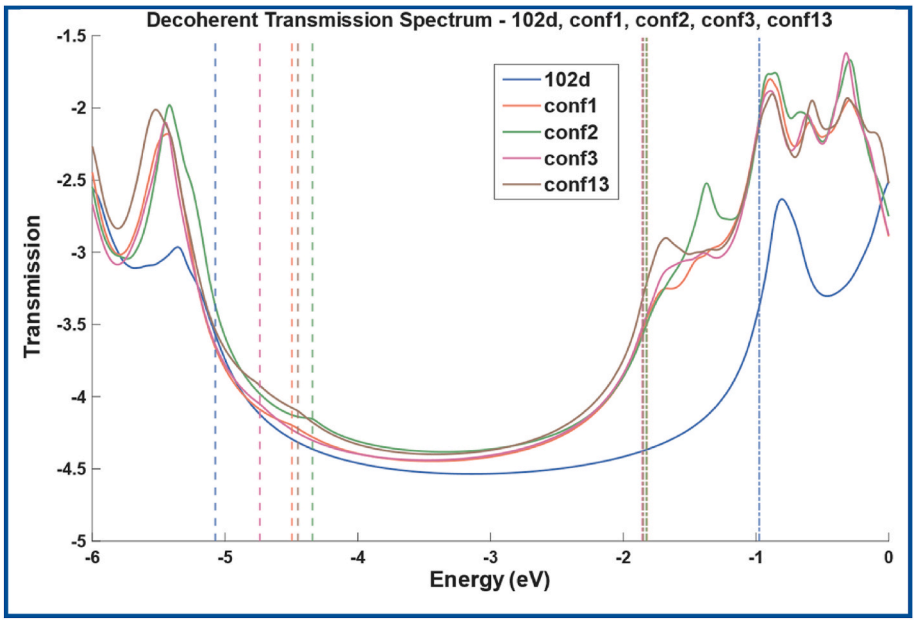

Fig. 6. Decoherent transmission spectra $T_{eff}(E)$ of the bare DNA (102d) and ligand–DNA complexes (conf1, conf2, conf3, and conf13), calculated using NEGF with Büttiker probes. The bare DNA shows weak delocalized resonances, while ligand binding suppresses transmission and promotes orbital localization.

that of the bare 102d duplex. These findings underline that ligand–DNA interactions exert a direct and strong influence not only on the structural but also on the electronic transport properties of DNA.

The density of states (DOS) profiles of the bare DNA duplex (102d) and four ligand–DNA complexes (conf1, conf2, conf3, and conf13) provide detailed insights into how ligand binding alters the electronic structure around the HOMO level (Figs. 7–11). In the bare 102d system, the HOMO region exhibits a relatively high total DOS value of approximately 11.6, almost entirely dominated by purine contributions (~10.3), with only a minor contribution from pyrimidines (~1.3). This result confirms that in the absence of ligands, the frontier orbitals are delocalized along the purine bases, consistent with earlier reports that identified purine–rich regions as the primary channels for charge transport in DNA [4,5].

In conf1, where the ligand intercalates at the terminal base pairs (1–24/2–23), the total DOS in the HOMO vicinity decreases sharply to 3.76, reflecting a threefold reduction compared to the bare duplex. Importantly, more than half of this contribution (Ligand DOS ≈ 1.95, ~52 %) arises directly from the ligand, while purine and pyrimidine contributions are reduced to 1.16 and 0.66, respectively. This redistribution highlights that terminal binding disrupts π–stacking and shifts the electronic density from DNA bases toward the ligand orbitals.

In conf2, with ligand intercalation deeper in the duplex (6–19/7–18), the total DOS near the HOMO is 3.60, very similar to conf1, yet the ligand contribution reaches ~1.94 (~54 % of the total), surpassing both purines (1.06) and pyrimidines (0.61). This pronounced localization

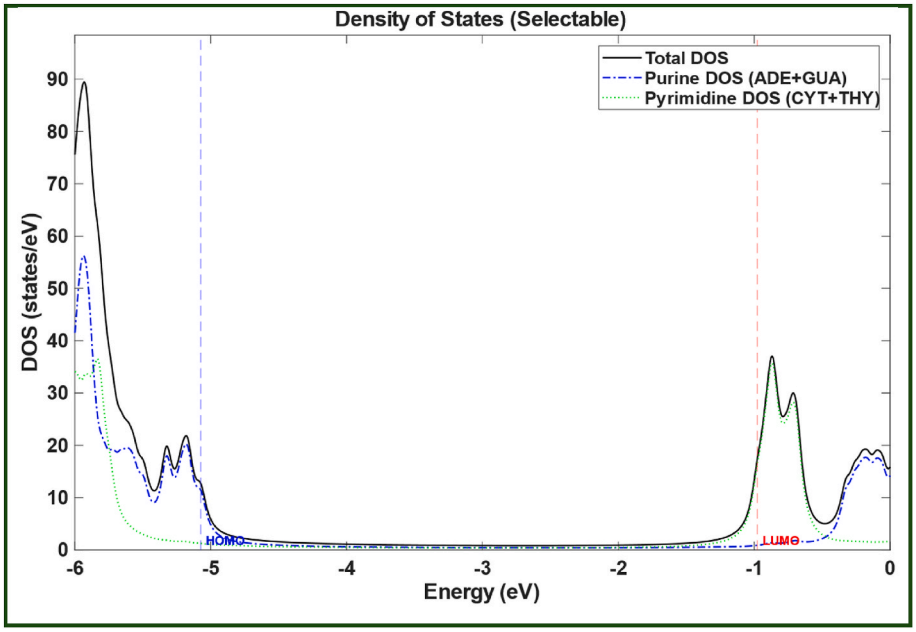

Fig. 7. DOS of bare DNA (102d) near the HOMO region. The high total density (~11.6) is dominated by purine contributions, reflecting delocalized orbital distribution.

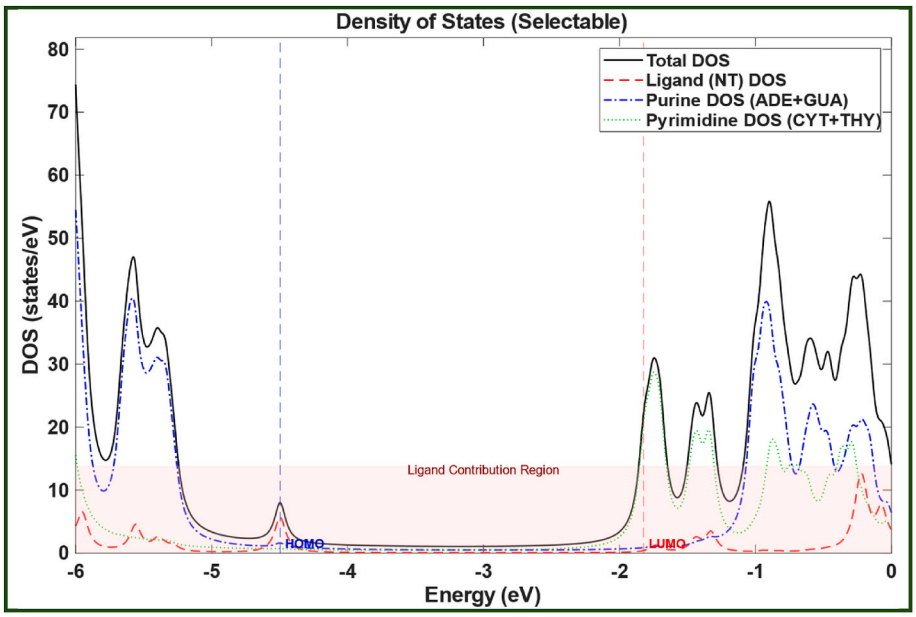

Fig. 8. DOS of conf1. The total density decreases to ~3.8, with ~52 % of the HOMO localized on the ligand and DNA contributions strongly reduced.

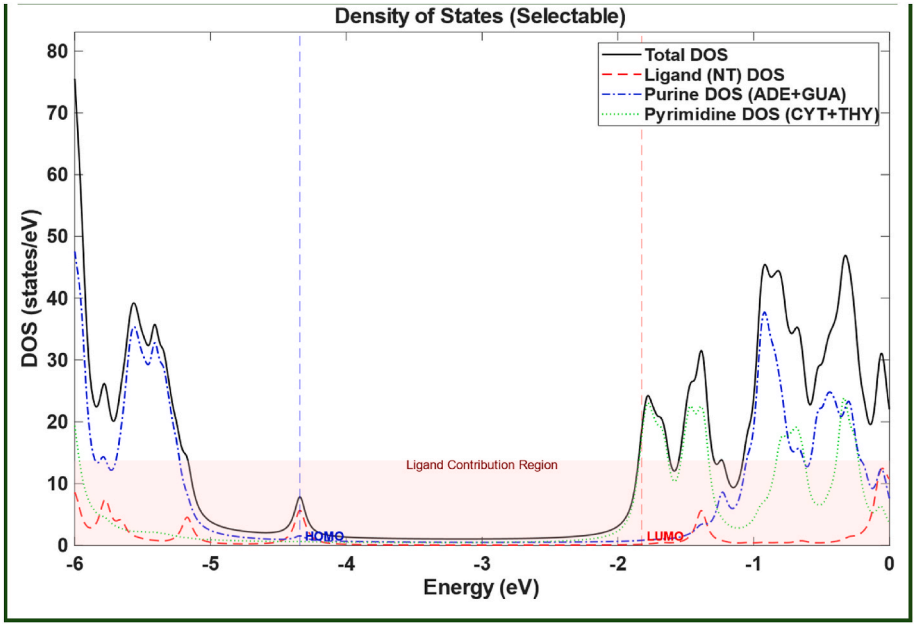

Fig. 9. DOS of conf2. The total density (~3.6) is dominated by ligand contributions (~54 %), indicating strong HOMO localization on the ligand.

indicates that the ligand orbitals dominate the HOMO region, supporting the notion that central intercalation has a stronger effect on frontier orbital redistribution than terminal binding.

The conf3 configuration, involving ligand binding at base pairs 11–14/12–13, shows a total DOS of 4.25. Here, the ligand contribution is ~2.11 (~50 %), while purines contribute ~1.37 and pyrimidines ~0.77. This profile suggests a hybrid character, where both ligand and DNA bases contribute significantly to the HOMO states. Compared to conf1 and conf2, conf3 retains a relatively higher DNA contribution, indicating that intercalation near the central region produces partial, but not complete, ligand dominance.

In conf13, with dual ligand binding at both termini (1–24/2–23 and 11–14/12–13), the total DOS is 4.04. The ligand contribution is the highest among all complexes (2.26, ~56 %), while purine and pyrimidine contributions remain suppressed at 1.13 and 0.65, respectively. This dual binding scenario produces the strongest suppression of DNA–based delocalization, as both ends of the duplex are blocked by ligands, confining HOMO orbitals almost entirely to the ligand sites.

Taken together, the DOS analysis demonstrates a systematic trend: the bare 102d DNA maintains a delocalized electronic structure dominated by purines, whereas all ligand–bound systems show (i) a reduction of the total DOS near the HOMO by approximately a factor of three, and (ii) a redistribution of orbital density in favor of the ligand. The range of conf1 (~52 % ligand contribution), to conf2 (~54 %), to conf3 (~50 %), and finally conf13 (~56 %) confirms that ligand binding not only suppresses delocalization but also enforces localization of HOMO orbitals on the ligand. These results are consistent with previous theoretical and experimental findings, which demonstrated that intercalating ligands perturb the intrinsic electronic structure of DNA, disrupt π–stacking, and suppress charge transport channels [5,11]. By directly correlating DOS

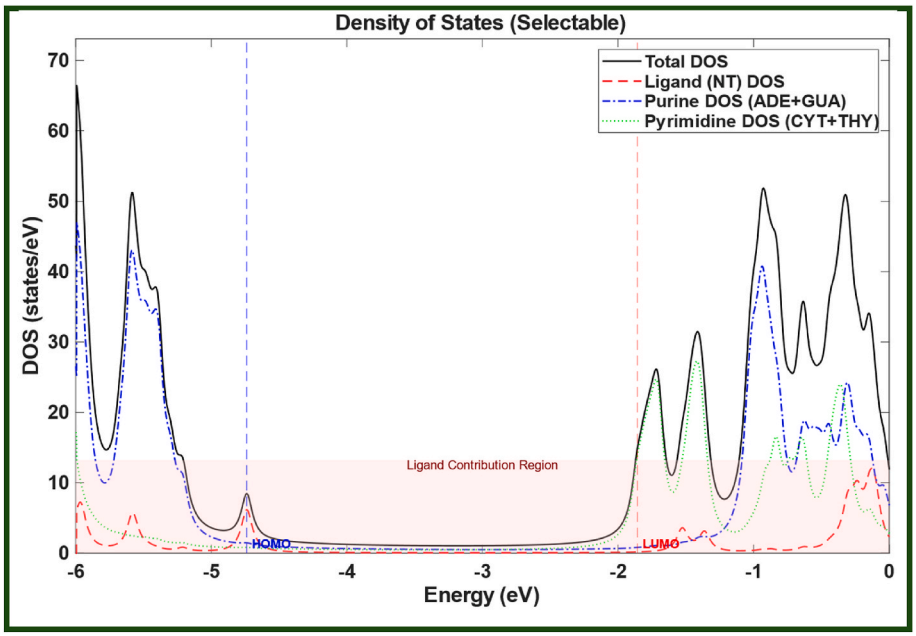

Fig. 10. DOS of conf3. The total density (~4.3) shows nearly equal ligand (~50 %) and DNA contributions, suggesting partial delocalization is retained.

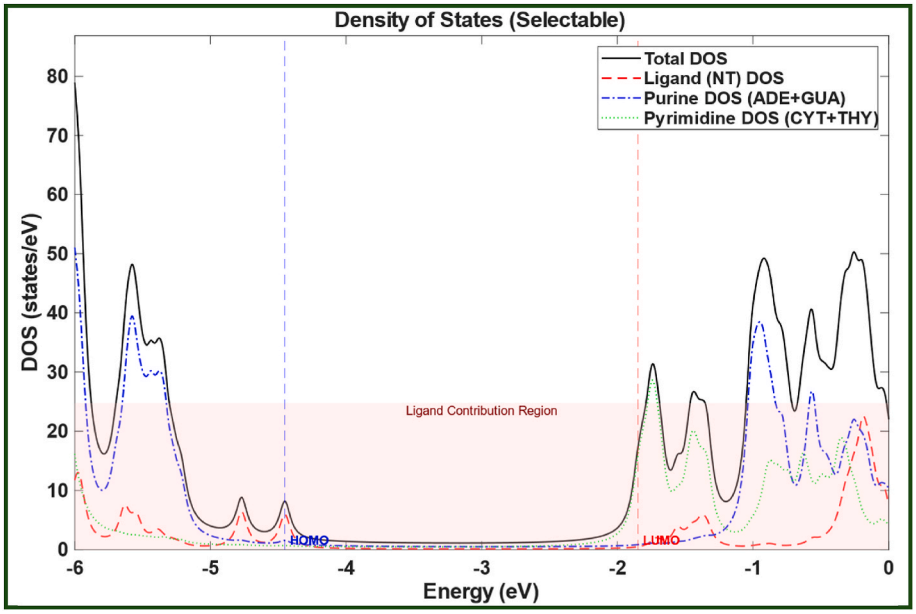

Fig. 11. DOS of conf13. The total density (~4.0) exhibits the strongest ligand dominance (~56 %), with HOMO orbitals largely localized on the ligands.

signatures with binding configurations, the present results establish that ligand binding systematically reduces DNA's intrinsic electronic conduction capacity and replaces it with ligand–centered orbital localization.

3.3. Effect of ligand functionalization on DNA electronic structure: DOS contour mapping

The Density of States (DOS) contour maps, supported by numerical data and molecular orbital calculations, provide a comprehensive understanding of the electronic perturbations induced by ligand functionalization. The DOS map of the pristine DNA system, serving as a reference (Reference Figure, left panel), exhibits the fundamental features of its electronic structure: a dense valence band spanning from approximately −5 eV to −6 eV with continuity across the base pairs, and a less defined conduction band above −2 eV. A vast forbidden energy gap of approximately 4 eV, characterized by a near–complete absence of states (deep blue), lies between these two primary bands. This visually corroborates the calculated 4.10 eV band gap between the HOMO at −5.07 eV and the LUMO at −0.98 eV. Upon ligand binding, this continuous HOMO-related band is replaced by one or more narrow in-gap features whose spectral weight is almost entirely concentrated on the ligand-bearing NT layers in the contour maps (Figs. 12, 14, 16 and 18), indicating that the HOMO orbitals become spatially localized around the ligands rather than remaining delocalized along the purine stack. This picture is quantitatively corroborated by the combined layer-resolved DOS bar plots (Figs. 13, 15, 17 and 19), which show that, at the HOMO energy, the DOS is overwhelmingly concentrated on the ligand sites with only minor leakage onto neighboring base pairs.

Each configuration created by the addition of the ligand perturbs this

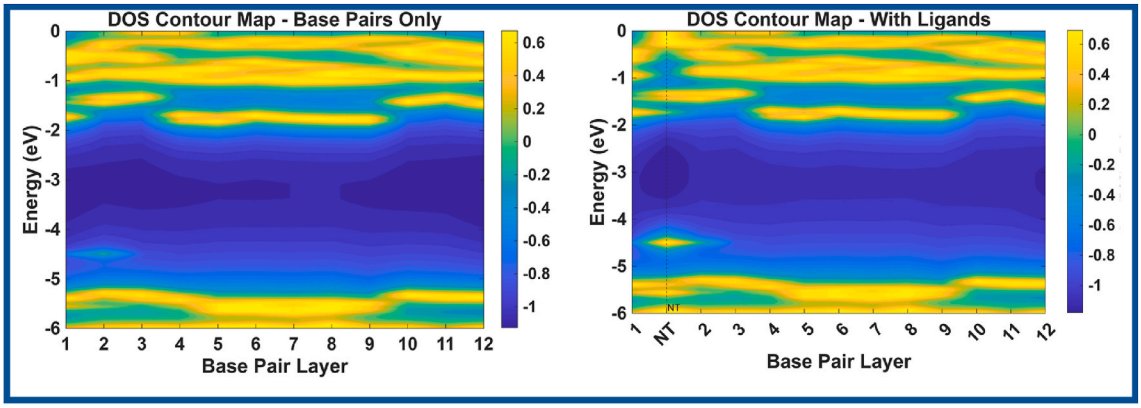

Fig. 12. DOS contour maps for the pristine 102d duplex (left) and conf1 (right), with a single NT ligand intercalated between the first two base–pair layers (L1–L2) at the starting terminus of the DNA duplex. In conf1, a narrow in–gap state appears around −4.50 eV, localized almost exclusively on the ligand (NT) column.

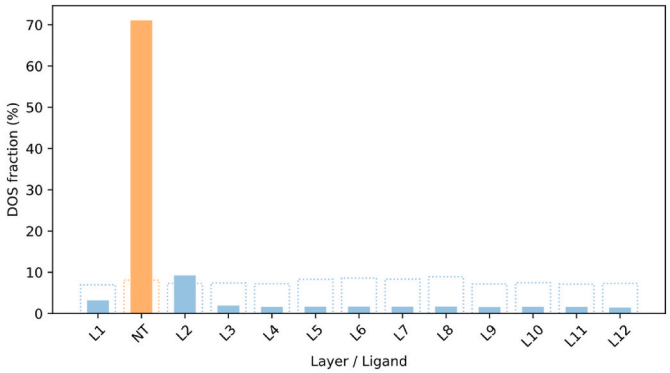

Fig. 13. Combined layer-resolved integrated DOS and HOMO-resolved DOS for conf1. For each layer, the dotted-outline bars indicate the integrated DOS over the −6.0 to 0.0 eV energy range, while the filled bars show the DOS fraction at the ligand HOMO energy (∼−4.50 eV. Blue bars correspond to DNA base-pair layers (L1–L12), and the orange bar to the NT ligand intercalated between L1 and L2. The integrated DOS remains distributed across the DNA stack, whereas at the HOMO the DOS is strongly localized on the ligand and its nearest base pair, confirming the trap-state character of the NT orbital.

fundamental electronic structure in a unique yet thematically consistent manner. The DOS map and its associated numerical data for each configuration provide detailed insight into the nature of this mechanism:

3.4. Quantitative analysis of Conf1 and Conf3: terminal effects and electronic isolation with numerical proof

Our comparative analysis of the single–ligand configurations (conf1 and conf3) provides conclusive evidence of a symmetry in electronic localization. The DOS contour maps for conf1 and conf3 (Figs. 12 and

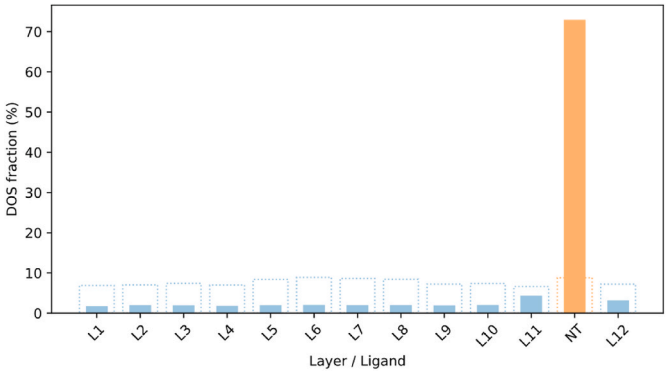

Fig. 15. Combined layer-resolved integrated DOS and HOMO-resolved DOS for conf3. For each layer, the dotted-outline bars indicate the integrated DOS over the −6.0 to 0.0 eV energy range, while the filled bars show the DOS fraction at the ligand HOMO energy (∼−4.73 eV). Blue bars correspond to DNA base-pair layers (L1–L12), and the orange bar to the NT ligand intercalated between L11 and L12 at the opposite terminus of the duplex. As in conf1, the integrated DOS remains DNA-dominated, whereas at the HOMO the DOS is strongly localized on the terminal ligand, confirming its trap-state character.

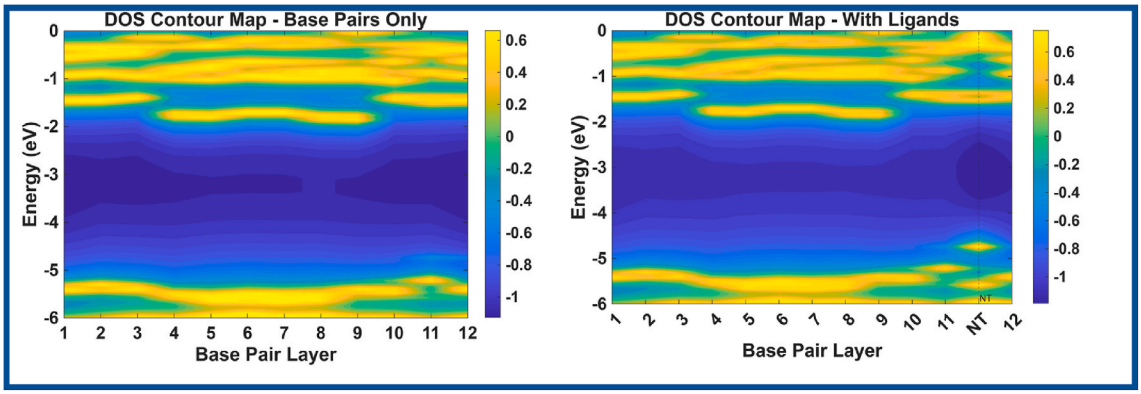

Fig. 14. DOS contour maps for the pristine 102d duplex (left) and conf3 (right), with a single NT ligand intercalated between the last two base–pair layers (L11–L12) at the ending terminus of the DNA duplex. In conf3, a narrow in–gap state appears around −4.74 eV, localized almost exclusively on the ligand (NT) column.

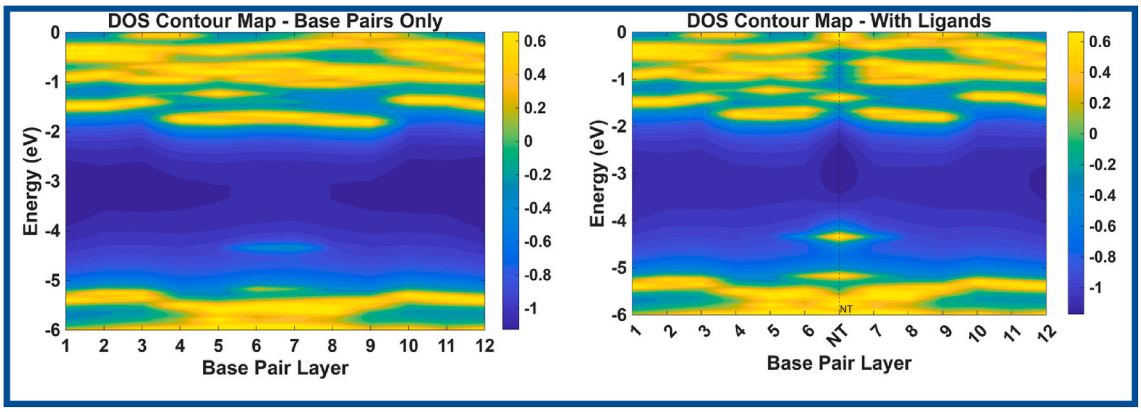

Fig. 16. DOS contour maps for the pristine 102d duplex (left) and conf2 (right), with a single NT ligand intercalated between the sixth and seventh base–pair layers (L6–L7) in the central region of the DNA duplex. In conf2, a symmetric narrow in–gap state appears around −4.34 eV, localized almost exclusively on the ligand (NT) column.

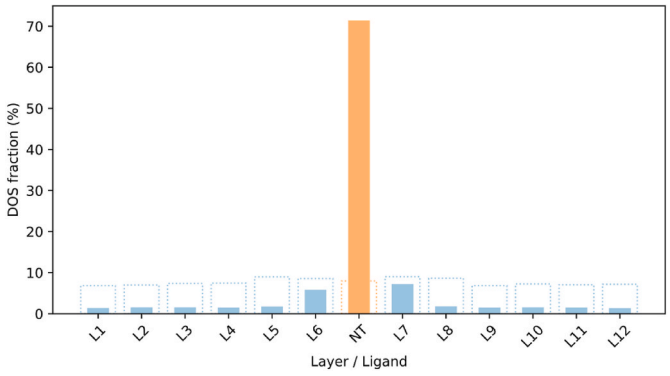

Fig. 17. Combined layer-resolved integrated DOS and HOMO-resolved DOS for conf2. For each layer, the dotted-outline bars indicate the integrated DOS over the −6.0 to 0.0 eV energy range, while the filled bars show the DOS fraction at the ligand HOMO energy (~−4.33 eV). Blue bars correspond to DNA base-pair layers (L1–L12), and the orange bar to the NT ligand intercalated between L6 and L7. The integrated DOS remains largely DNA-dominated, whereas at the HOMO the DOS is sharply localized on the central ligand, confirming its role as a deep trap state.

14, respectively), together with the corresponding layer-integrated DOS bar plots (Figs. 13 and 15), show that despite binding at opposite termini of the duplex, both systems exhibit a localized “trap-state” mechanism. For conf1, quantitative analysis at the HOMO energy (−4.49 eV) reveals a ligand DOS of 5.67 compared to an average DNA DOS of 0.19, yielding a localization ratio of ~29.5. Remarkably, conf3 mirrors this behavior almost exactly: at its HOMO energy (−4.73 eV), the ligand DOS reaches 6.01, while the DNA backbone retains a minimal average DOS of 0.19, resulting in a similar localization ratio of ~31.9. Although a slight local elevation in DOS is observed at the intercalation site in conf3 (specifically base pairs L11 and L12, peaking at 0.36), it is negligible compared to the ligand’s dominance. This consistent ~30-fold difference across both configurations confirms that the ligand orbitals only weakly hybridize with the DNA π-stack and do not form an extended conductive channel. Instead, they give rise to narrow, high-amplitude resonances localized on the ligand, which explains the apparent paradox of high transmission peaks coexisting with strongly suppressed macroscopic conductance.

3.5. *Characterization of Conf2: the numerical nature of an embedded trap*

In this single-ligand configuration (conf2), the NT ligand is intercalated in the central region of the 102d duplex, specifically between the 6th and 7th base-pair layers (L6–L7). The system exhibits the narrowest band gap (2.52 eV). The DOS contour map (Fig. 16) reveals a symmetric and highly intense in-gap state at approximately −4.33 eV, centered on the ligand column. This observation is corroborated by the raw DOS data: at the ligand HOMO energy (~−4.33 eV), the DOS contribution from the ligand reaches ~5.3, whereas the DNA base pairs remain much smaller. Even at the adjacent layers L6 and L7, the DOS peaks at only

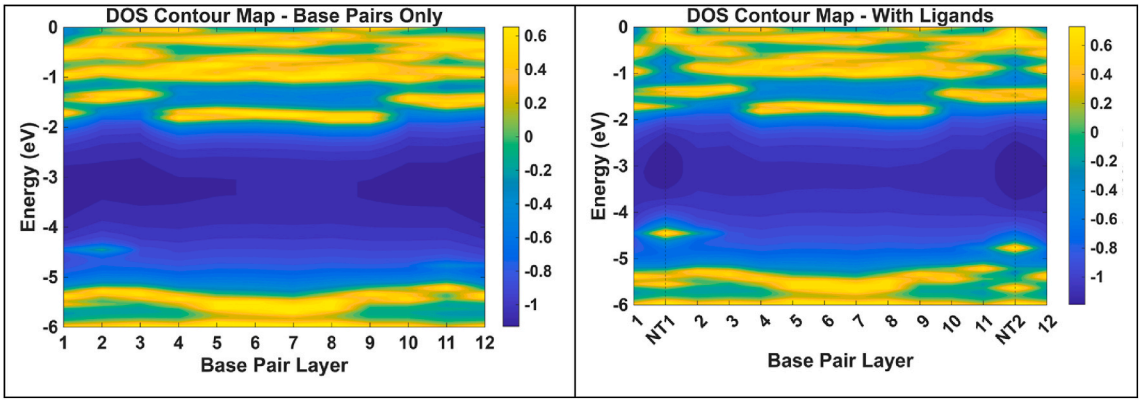

Fig. 18. DOS contour maps for the pristine 102d duplex (left) and conf13 (right), with two NT ligands bound at opposite termini of the duplex, intercalated between the first two (L1–L2) and the last two (L11–L12) base–pair layers (NT1 and NT2). In conf13, two narrow in–gap states appear around −4.45 eV, localized almost exclusively on the ligand (NT1 and NT2) columns, while the DOS on the intervening DNA base–pair layers (L1–L12) remains vanishingly small.

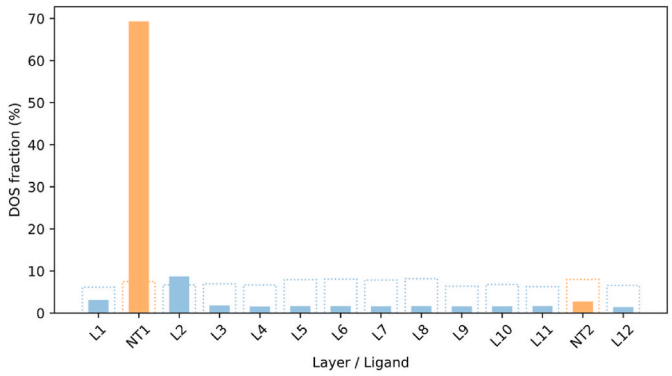

Fig. 19. Combined layer-resolved integrated DOS and HOMO-resolved DOS for conf13. For each layer, the dotted-outline bars indicate the integrated DOS over the −6.0 to 0.0 eV energy range, while the filled bars show the DOS fraction at the ligand HOMO energy (~−4.44 eV). Blue bars correspond to DNA base-pair layers (L1–L12), and the orange bars to the two ligands NT1 (between L1–L2) and NT2 (between L11–L12). The integrated DOS reveals comparable total contributions from NT1 and NT2 (~7–8% each), whereas at the HOMO the DOS is strongly localized on NT1 at the L1–L2 interface, consistent with a terminal trap state.

~0.6, while more distant base pairs stay around ~0.1. This substantial contrast—nearly an order of magnitude relative to the nearest neighbors and ~30-fold relative to the DNA average—demonstrates that the HOMO is predominantly confined to the ligand rather than being delocalized along the DNA chain. The layer-integrated DOS analysis in Fig. 17 further supports this picture: over the whole energy window the ligand carries only ~8 % of the total DOS, comparable to a single base pair, while the central base-pair layers (L5–L8) contribute ~9 % each and the remaining layers contribute ~7 %. Together, Figs. 16 and 17 show that the NT ligand forms a deep, localized potential well within the base stack, effectively acting as a trap state that hinders charge transport.

3.6. Quantitative analysis of Conf13: conclusive visual and numerical proof of Non–Conductivity

This system, with ligands attached to both termini of the DNA helix, provides the most definitive evidence for the localization and non–conductivity hypothesis. The DOS map clearly shows two discrete, energetically degenerate, but spatially disconnected high–density states within the band gap at approximately −4.45 eV (Fig. 18).

As visually confirmed by the 3D isosurface plot in Fig. 4, the HOMO orbital in the conf13 system is strictly localized at the upper terminal of the duplex. This spatial distribution is in excellent agreement with the DOS calculations, which indicate that charge density is concentrated primarily on the first ligand (NT1) intercalated between the L1 and L2 base pairs; the layer-integrated DOS bar plot in Fig. 19 further confirms the dominance of NT1 and the negligible contribution from the second ligand. While NT1 exhibits a dominant DOS contribution of ~5.49, the second ligand positioned downstream remains electronically inactive (DOS ~0.23), displaying no significant orbital density. Furthermore, the isosurface clearly depicts the orbital cloud extending slightly onto the adjacent L2 base pair, corroborating its elevated DOS value (~0.71). This confirms that, despite the presence of two ligands, the system undergoes severe symmetry breaking, where the charge is trapped exclusively within the potential well of the NT1 ligand at the L1–L2 interface.

These individual and detailed analyses converge on a singular conclusion: the NT ligand, irrespective of its binding position or number, acts as a highly effective **"charge sink"** or **"electron trap."** Specifically, the intercalation of the ligand creates a deep potential well that breaks the structural and electronic symmetry required for resonant transport. Such localized states, despite being energetically favorable, are known to impede charge mobility, a phenomenon widely reported in both DNA systems [46–48] and in the broader field of organic semiconductors [49, 50].

In conclusion, while the addition of the NT ligand successfully narrows the system's energy gap and introduces new states into the band gap, the extreme localization character of these states–observed in the contour maps and confirmed by the numerical data–creates a detrimental effect on charge transport. This work underscores that in the design of functional molecular electronic components, not only are the energy levels of the molecular orbitals critical, but so too is their spatial distribution (localization vs. delocalization). An effective molecular wire design necessitates not only a narrow band gap but also the seamless delocalization of frontier orbitals along the conductive pathway.

3.7. Electronic transport and conductance behavior of DNA–ligand complexes

The evaluation of conductance in pristine and ligand–functionalized DNA duplexes provides direct insights into how ligand binding perturbs charge transport. In all transport calculations, the Fermi level (E_F) was positioned close to the HOMO band of the purine stack, in agreement with the widely accepted picture that charge migration in DNA is dominated by hole conduction. For the bare 102d duplex, the HOMO is located at −5.07 eV, with a conductance of $G \approx 2.685 \times 10^{-4}$ G_0 (Table 2). This value indicates that the native π–stacking along the DNA bases provides a limited yet measurable conduction pathway, consistent with earlier findings that guanine–rich DNA supports long–range charge transport [46–48]. In the ligand–bound systems, however, the HOMO density is partially shifted and localized onto the ligand, giving rise to narrow ligand–centered resonances that do not coincide with E_F. As a consequence, the effective transmission at the Fermi level, Teff(E_F), and therefore the zero–bias conductance, are reduced by 67–76 % in all ligand–bound configurations, even though their maximum transmission peaks exceed those of the bare duplex.

Conf1, with a terminally bound ligand, shows a HOMO at −4.49 eV and a conductance of 6.34×10^{-5} G_0, corresponding to ΔG = −76.39 % (Table 2). As illustrated in Fig. 20, the conductance curve of conf1 is systematically suppressed relative to bare DNA, and the HOMO vertical line highlights orbital localization on the ligand rather than on the DNA strand.

Conf2, featuring a centrally intercalated ligand, presents the narrowest band gap (2.51 eV) but only a conductance of 7.00×10^{-5} G_0 (ΔG = −73.92 %). This suppression, visualized in Fig. 21, is directly tied to the emergence of a deep trap state around −4.34 eV, confirmed by the conductance profile and the corresponding transmission spectrum. Despite its position within the dense π–stacking region, the HOMO orbital remains localized on the ligand, isolating it electronically from neighboring base pairs.

Conf3, with a ligand intercalated at the opposite terminal base-pair region, exhibits a HOMO at −4.74 eV and the largest conductance among the functionalized systems, 8.87×10^{-5} G_0 (ΔG = −66.95 %). As shown in Fig. 22, the suppression at the HOMO level is noticeable but

Table 2
Summary of calculated HOMO energies, conductance values (G), and relative conductance reductions (ΔG) for the pristine DNA duplex (102d) and ligand–functionalized systems. Values clearly show that ligand binding shifts HOMO levels upward and consistently suppresses conductance compared to the bare DNA reference.

System	HOMO(eV)	Bandgap(eV)	Conductance (G_0)	ΔG(%)
102d	−5.07	4.09	2.685e–04	–
conf1	−4.49	2.67	6.340e–05	−76.39
conf2	−4.34	2.51	7.002e–05	−73.92
conf3	−4.73	2.88	8.874e–05	−66.95
conf13	−4.45	2.60	7.955e–05	−70.37

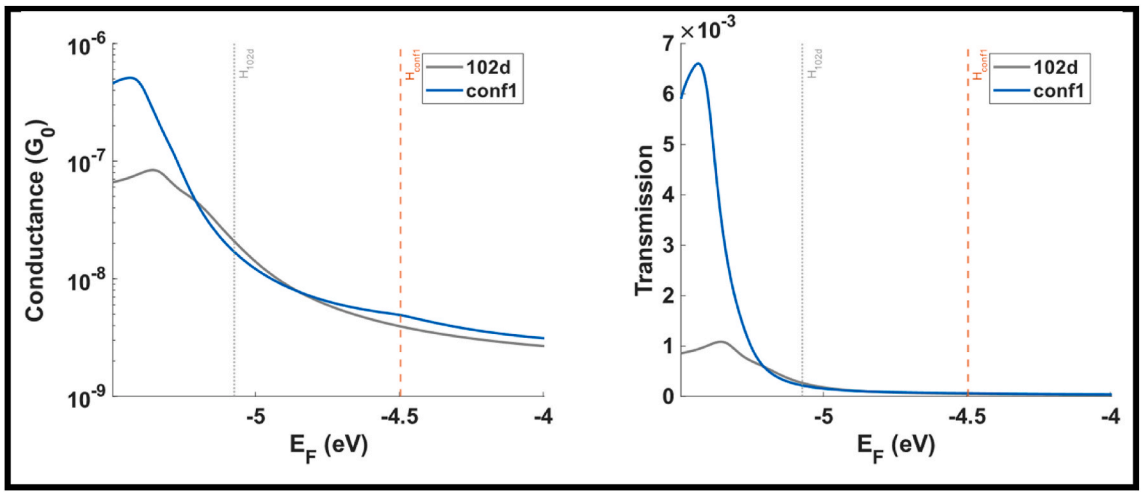

Fig. 20. Comparison of conductance (left) and transmission (right) for 102d and conf1. Dashed vertical lines indicate the HOMO energy levels.

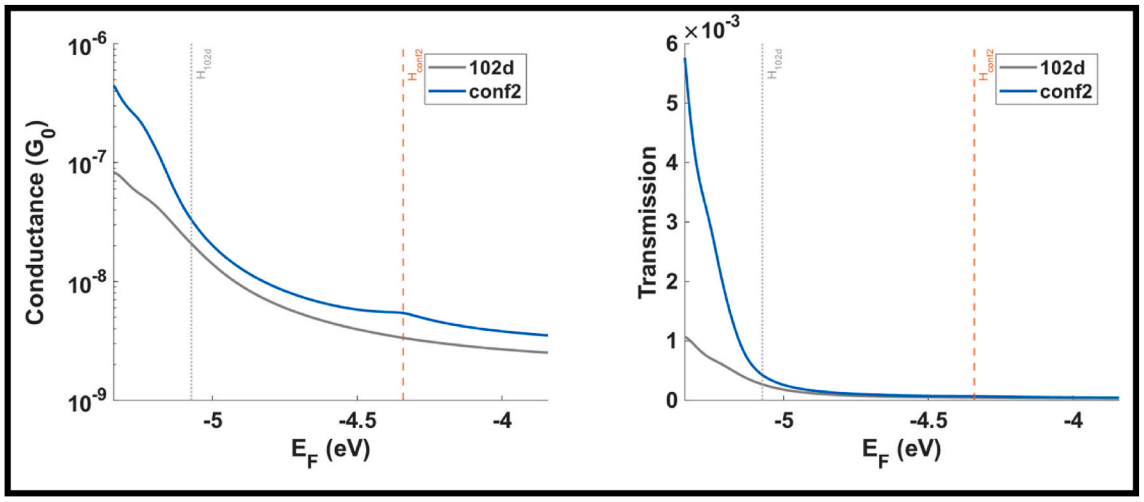

Fig. 21. Comparison of conductance (left) and transmission (right) for 102d and conf2. Dashed vertical lines indicate the HOMO energy levels.

comparatively less severe.

Conf13, where ligands are positioned at both termini, has a HOMO at −4.45 eV and a conductance of 7.95×10^{-5} G_0 ($\Delta G = -70.37$ %). The corresponding graph (Fig. 23) demonstrates two ligand–localized states without any electronic bridging across the intervening DNA, indicating that the backbone no longer behaves as an efficient molecular wire when

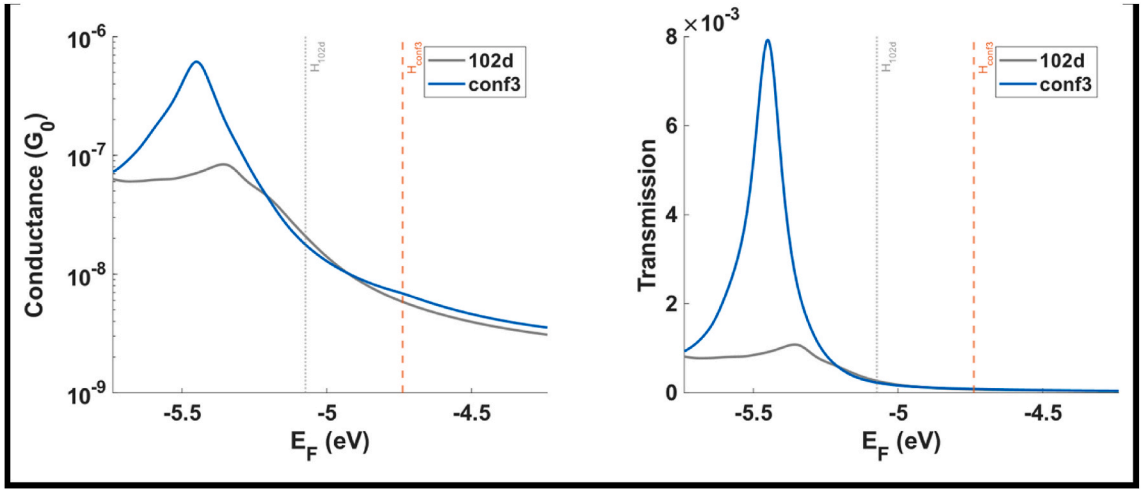

Fig. 22. Comparison of conductance (left) and transmission (right) for 102d and conf3. Dashed vertical lines indicate the HOMO energy levels.

both ends are ligand–terminated.

Collectively, these corrected values confirm that HOMO orbitals in all ligand–functionalized systems are spatially localized on ligands rather than delocalized across DNA bases. This localization suppresses conduction even as the HOMO–LUMO gap is reduced, producing states that act as electron traps rather than transport channels. The overall behavior is consistent with decoherent transport frameworks and with broader literature emphasizing that sustained long–range transport in DNA requires HOMO delocalization [46–50].

In conclusion, the systematic suppression of conductance—quantified in Table 2 and visualized in Figs. 20–23—confirms that NT ligand binding disrupts the conductive pathway in DNA. While energy gaps are reduced, the loss of orbital delocalization renders the systems electronically less efficient, underscoring the critical importance of orbital spatial distribution in molecular wire design ($\Delta G \approx -66.9$ % to -76.4 %).

The $\ln(G/G_0)$–(E_F-E_{HOMO}) curves presented in Fig. 24 provide a complementary perspective on the conductance behavior of the 12–base pair 102d duplex and its ligand–bound variants. Employing the relative scale (E_F-E_{HOMO}) on the horizontal axis allows for a normalized comparison across systems, since the absolute HOMO positions vary but the relative energetic distance from the Fermi level governs the effective transport.

For the pristine duplex (102d), the conductance starts at $\ln(G/G_0) \approx -8.1$ ($G/G_0 \approx 3 \times 10^{-4}$) and decreases to $\ln(G/G_0) \approx -9.2$ ($G/G_0 \approx 1 \times 10^{-4}$) at $E_F-E_{HOMO} = 0.5$ eV. This three–fold reduction reflects the intrinsic exponential decay of tunneling conductance with increasing energy separation.

In conf1, with ligand binding at the terminal base pairs, the initial conductance is $\ln(G/G_0) \approx -9.7$ ($G/G_0 \approx 6 \times 10^{-5}$), nearly five times lower than the bare DNA, and declines further to $\ln(G/G_0) \approx -10.2$ ($G/G_0 \approx 3.7 \times 10^{-5}$) at 0.5 eV conf2, featuring central intercalation at positions 6–19/7–18, exhibits an initial conductance of $\ln(G/G_0) \approx -9.5$ ($G/G_0 \approx 7.5 \times 10^{-5}$), corresponding to a four–fold reduction, and decreases to $\ln(G/G_0) \approx -10.1$ ($G/G_0 \approx 4 \times 10^{-5}$). conf3, with ligands intercalated at 11–14/12–13, shows $\ln(G/G_0) \approx -9.4$ ($G/G_0 \approx 8 \times 10^{-5}$) initially and $\ln(G/G_0) \approx -10.0$ ($G/G_0 \approx 4.5 \times 10^{-5}$) at 0.5 eV, representing a 3.5–fold suppression relative to the pristine duplex.

Conf13, which carries ligands at both termini (1–24/2–23 and 11–14/12–13), presents an intriguing case: despite dual binding, the initial conductance $\ln(G/G_0) \approx -9.3$ ($G/G_0 \approx 9 \times 10^{-5}$) is slightly higher than conf1 and conf2, amounting to a three–fold reduction relative to 102d. At 0.5 eV, the value converges to $\ln(G/G_0) \approx -10.0$ ($G/G_0 \approx 4.5 \times 10^{-5}$). This unexpected behavior suggests that dual terminal ligands partially stabilize base stacking at the ends of the duplex, redistributing HOMO density and thereby preserving limited conduction pathways.

Across all systems, $\ln(G/G_0)$ decreases monotonically with increasing E_F-E_{HOMO}, firmly indicating that tunneling is the dominant transport regime. These results align with prior reports underscoring the critical role of HOMO delocalization in DNA charge transport and its disruption by ligand binding [5,11]. Thus, while ligand functionalization narrows the bandgap, the associated orbital localization suppresses long–range charge mobility, a mechanism consistently observed in both experimental and theoretical studies.

3.8. Molecular dynamics simulations and binding free energy calculation via MM/GBSA

The binding free energy analysis was conducted to examine whether ligand binding strength is associated with the computationally observed suppression of electronic conductance in DNA–ligand systems. Specifically, these calculations assessed whether ligands occupying distinct intercalation or terminal binding sites display different binding stabilities and whether such variations are reflected in the modulation of charge-transport pathways.

The binding free energies (ΔG_{bind}) of the DNA–ligand complexes were calculated using the Molecular Mechanics/Generalized Born Surface Area (MM/GBSA) method based on equilibrated MD trajectories, with the entropic contribution estimated using the interaction entropy approach. The total binding free energy is expressed as [51–53]:

$$\Delta G_{bind} = G_{complex} - (G_{DNA} + G_{ligand}) \quad [24]$$

with each free energy term given by

$$G = E_{MM} + G_{solvation} - TS \quad [25]$$

where E_{MM} is the molecular mechanics energy, $G_{solvation}$ is the solvation free energy, and TS is the entropic contribution. The molecular mechanics energy is further decomposed into bonded, van der Waals, and electrostatic interactions:

$$E_{MM} = E_{bonded} + E_{vdW} + E_{ele} \quad [26]$$

The solvation free energy was divided into polar and nonpolar terms,

$$Gs_{olvation} = G_{polar} + G_{nonpolar} \quad [27]$$

where the polar contribution was estimated within the Generalized Born framework (igb = 5), while the nonpolar term was calculated from the solvent–accessible surface area (SASA). The entropic contribution was estimated using the interaction entropy approximation, which has been

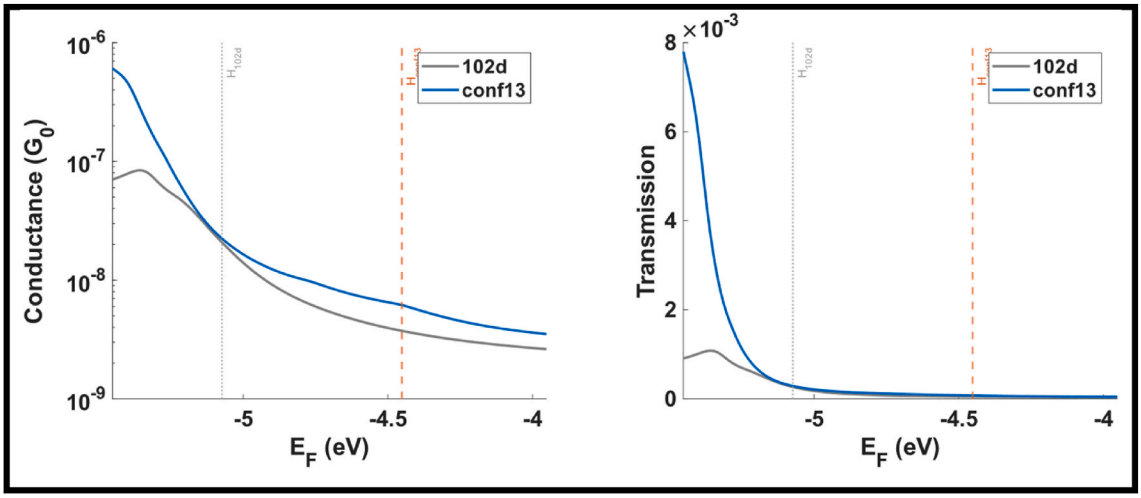

Fig. 23. Comparison of conductance (left) and transmission (right) for 102d and conf13. Dashed vertical lines indicate the HOMO energy levels.

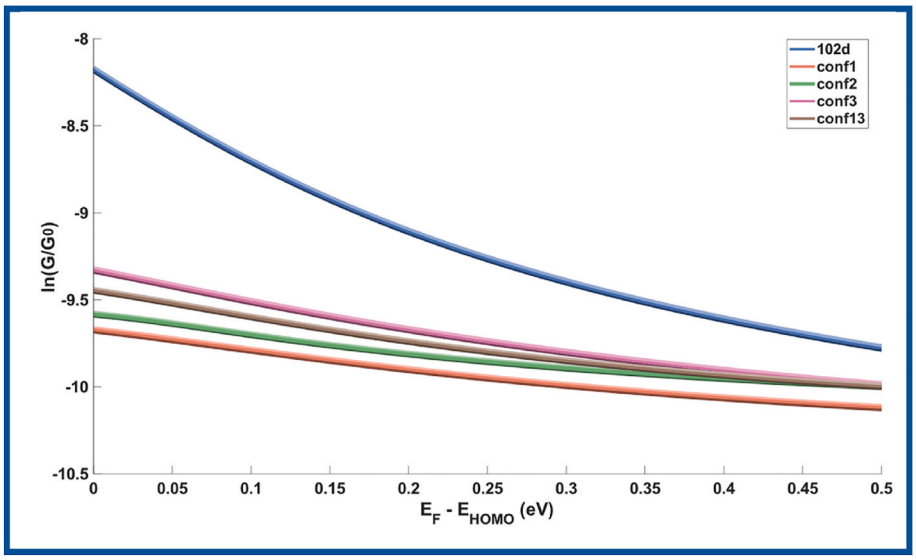

Fig. 24. Quantum conductance spectra of the bare 102d duplex and its ligand–bound variants (*conf1*, *conf2*, *conf3, conf13*). The vertical axis shows $\ln(G/G_0)$, while the horizontal axis corresponds to $E_F - E_{HOMO}$ (eV).

shown to improve agreement with experimental data for DNA–ligand systems [54].

Using the MD trajectories obtained as described in Section 2.4 and the protocol summarized in Section 2.5, MM/GBSA calculations were performed with gmx_MMPBSA v1.6.0 in combination with GROMACS 2024.4 following our previous protocol [1,7]. Frames were extracted every 10 ps over the last 50 ns of each production run, yielding ~5000 snapshots per system (Fig. 25).

This methodology, which has also been adopted in recent studies of nucleic acid–ligand systems [9], provides a consistent framework for estimating binding affinities and for correlating ΔG_{bind} trends with the computed electronic conductance behavior of DNA–ligand complexes.

Molecular dynamics simulations were used to probe the time-dependent structural stability of the bare DNA duplex and its ligand–-bound variants and to identify conformational features that may influence charge transport. Representative structures were examined at 0, 25, and 50 ns, focusing on DNA backbone deformation, purine-path continuity, and the persistence of ligand–DNA interactions with specific nucleotide residues. In this analysis, three complementary structural indicators were used to quantify the stability of the ligand–DNA complexes and to rationalize their transport properties. First, the root–mean–square deviation (RMSD) of the DNA backbone and the purine stack was monitored as a global measure of helix deformation. Second, the minimum distances between the ligand and the closest base residues (Table 3) were followed as a proxy for the persistence or loss of π–stacking contacts. Third, the effective length and continuity of the purine conduction pathway were derived from the number of purine steps and the average inter–base distance, as well as from the full distributions of purine path lengths (Figs. 26 and 27). Configurations that maintain low RMSD values, short ligand–base distances (~3–4 Å), and compact purine pathways (~55–58 Å) tend to preserve more favorable transmission channels, whereas systems that evolve toward larger RMSD (>3 Å), ligand detachment (>6–8 Å), and elongated or fragmented paths (up to ~80 Å) exhibit the strongest suppression of conductance relative to the bare 102d duplex.

For conf1, the ligand initially maintained a tight π–stacking interaction with the terminal guanine residue GUA24 at 0 ns, establishing close contact at 2.98 Å and preserving a continuous purine pathway of four effective steps (Fig. 26). By 25 ns, a pronounced disruption was observed: the backbone RMSD rose to 3.41 Å, the purine path shortened from four to three steps, and the ligand–DNA distance to GUA24 increased to 9.51 Å, indicating dissociation from the terminal residue. At 50 ns, the ligand approached CYT23 at ~7.0 Å but did not reestablish stable stacking; the purine ladder nominally returned to four steps, albeit with elongated inter–base distances (~7.9 Å). Overall, these results suggest that the major structural disruption occurs within the 0–25 ns window and remains only partially recovered at 50 ns, consistent with the suppressed conductance observed in the $\ln(G/G_0)$–$(E_F\text{-}E_{HOMO})$ profiles.

For conf2, the ligand was embedded near the central residues (around layers corresponding to bases 6–19 and 7–18) (Fig. 27). At 0 ns, the ligand was positioned in close π–stacking with adjacent adenine–guanine bases, preserving purine continuity. By 25 ns, partial separation from these central bases emerged, elongating local stacking

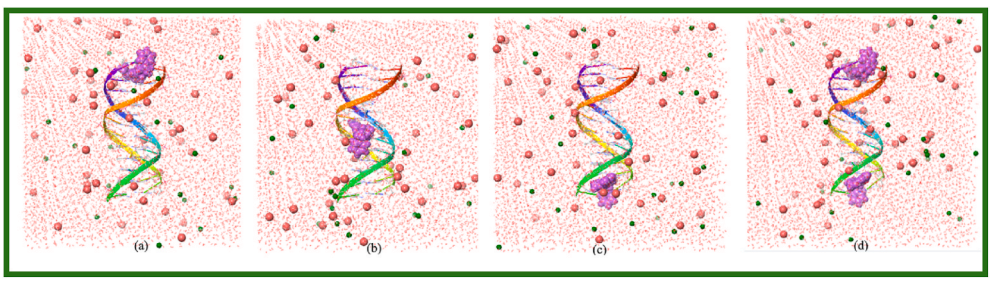

Fig. 25. Solvated DNA–ligand systems in explicit TIP3P water boxes with added K^+ and Cl^- ions for charge neutralization. The DNA duplex is shown as a rainbow–colored ribbon, ligands are highlighted in magenta space–filling representation, potassium ions (K^+) are shown as orange spheres, chloride ions (Cl^-) as green spheres, and water molecules as red sticks. Panels correspond to different DNA–ligand complexes: (a) conf1, (b) conf2, (c) conf3, and (d) conf13.

Table 3
Time evolution of ligand–DNA contacts and purine path continuity in the four configurations (conf1, conf2, conf3, conf13). Distances correspond to the ligand center of mass to the nearest base residue; purine path continuity is expressed as number of effective steps and average inter–base distance ⟨d⟩.

System	0 ns (Residue/Distance, Å)	Purine path (steps/⟨d⟩, Å)	25 ns (Residue/Distance, Å)	Purine path (steps/⟨d⟩, Å)	50 ns (Residue/Distance, Å)	Purine path (steps/⟨d⟩, Å)
conf1	GUA24 – 2.98 Å (tight π–stacking at terminal)	4/7.43	GUA24 – 9.51 Å (ligand detached)	3/7.91	CYT23 – 7.01 Å (partial proximity)	4/7.90
conf2	Central purines ADE/GUA ~3.2 Å (stable stacking)	5/7.12	ADE19/GUA18 – 6.5 Å (weakened contacts)	4/7.85	ADE19/GUA18 – 5.9 Å (ligand remains in groove)	4/7.80
conf3	ADE12/GUA13 – 3.4 Å (mid–helix insertion)	5/7.21	ADE12/GUA13 – 5.7 Å (reduced overlap)	4/7.88	ADE12/GUA13 – 6.2 Å (persistent misalignment)	4/7.95
conf13	GUA1 – 3.1 Å; GUA24 – 2.9 Å (both termini stabilized)	5/7.18	GUA1 – 7.4 Å; GUA24 – 8.1 Å (ligands separated)	3/8.10	CYT2 – 6.8 Å; CYT23 – 7.2 Å (termini fragmented)	3/8.05

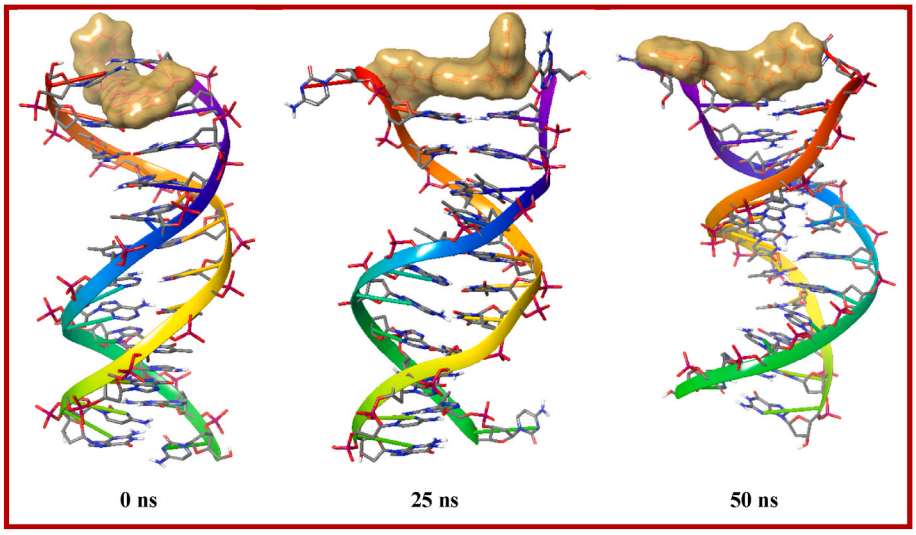

Fig. 26. Snapshots of conf1 system at 0, 25, and 50 ns, showing conformational changes and ligand stabilization within the major groove during the simulation.

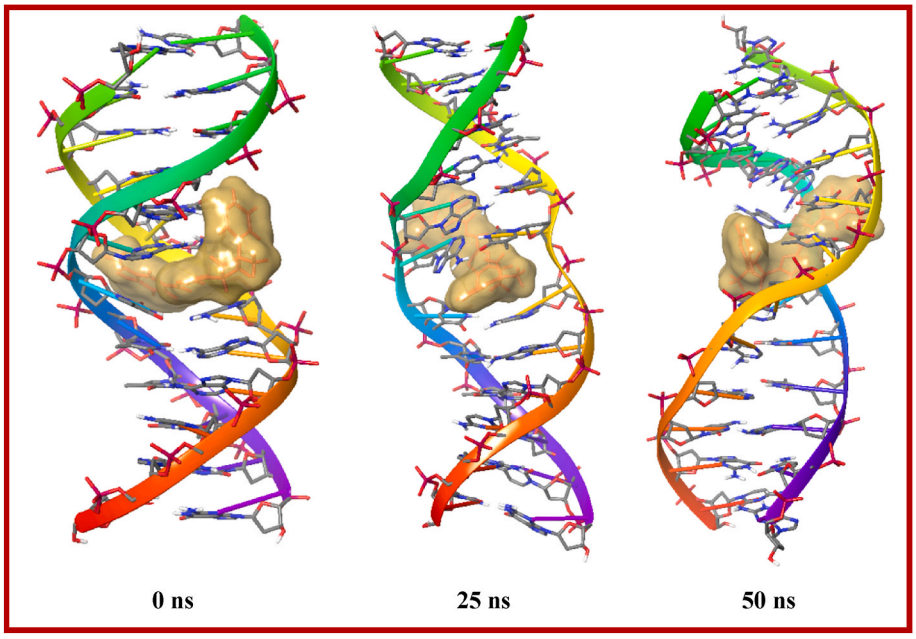

Fig. 27. Snapshots of conf2 system at 0, 25, and 50 ns, showing conformational changes and ligand stabilization within the major groove during the simulation.

distances. At 50 ns, the ligand remained localized within the central groove and maintained contact with nearby residues, yet prevented effective overlap with neighboring purines. This provides a structural basis for why conf2, despite its computed narrower band gap, exhibits reduced conductance.

For conf3, the ligand intercalated near the mid–helix (close to bases

11–14/12–13) remained tightly associated at the start (Fig. 28). By 25 ns, structural deviation emerged in this region, with the ligand slightly shifting away from its initial π–stacked partners. At 50 ns, the RMSD increased further; although the ligand continued to interact with the same central residues, the purine pathway remained partially disrupted, limiting efficient electronic delocalization along the helix.

For conf13, both termini were initially stabilized by ligand–base contacts (NT1 near GUA1 and NT2 near GUA24). By 25 ns, both ligands simultaneously weakened their strong stacking interactions, moving away from their respective guanine residues and creating fragmented ends (Fig. 29). At 50 ns, the ligands remained displaced (~6–8 Å), and the intervening DNA residues did not recover purine path continuity. This dual terminal disruption supports the severe suppression of charge transport observed in this system.

When compared with the bare 102d duplex, all ligand–bound systems demonstrate a consistent mechanism: pristine DNA maintains HOMO delocalization along stacked purines, whereas ligand binding disrupts residue–specific stacking (GUA24, CYT23, and mid–helix adenine/guanine sites), leading to localization of electronic states on the ligand and reduced conductance (Table 3). These residue–level observations align with the overall decrease in conductance relative to 102d, indicating that ligand–induced π–stacking disruption and residue disengagement play central roles in suppressing charge transport.

The statistical analysis of purine pathway lengths (Fig. 30) provides further insight into the structural dynamics summarized in Table 3. The overlaid histograms reveal that conf2 is the most compact system, with a sharply peaked distribution centered at 56.9 ± 2.2 Å and a narrow range (50.7–70.4 Å), consistent with the persistence of a locally confined intercalative state. conf1 and conf3 exhibit comparable averages (58.2 ± 3.6 Å and 58.2 ± 3.4 Å, respectively) and intermediate ranges (~50–69 Å), indicating moderate fluctuations in which local disruptions are counterbalanced by partial re-stacking events. In contrast, conf13 shows a broad and right-shifted distribution with a mean of 65.5 ± 4.6 Å extending up to 80.9 Å, reflecting pronounced elongation of the purine track and enhanced conformational heterogeneity.

The kernel density plots in Fig. 30 reinforce these trends, showing a narrow, high-amplitude peak for conf2, broader intermediate peaks for conf1 and conf3, and a wide, flattened distribution for conf13. The box plot comparison further highlights these differences, with conf2 presenting the lowest interquartile range, conf1 and conf3 occupying intermediate positions, and conf13 displaying the highest median and widest spread. Collectively, these distributional data and the accompanying structural metrics summarized in Table 3 indicate that ligand binding modulates not only the mean pathway length but also the conformational flexibility of the purine stack. Systems with compact and narrow distributions (e.g., conf2) are expected to exhibit more consistent charge transport, whereas broadened and elongated pathways (e.g., conf13) are indicative of disrupted stacking and reduced conductance.

The structural dynamics underlying these statistical distributions are elucidated in greater detail in Fig. 31. In this analysis, the centers of mass of the purine bases along the purine pathway are indexed by *i*; thus, the term i_{12} refers to the distance between the first and second purine bases on the path, i_{23} refers to the distance between the second and third, and so on. Fig. 31 illustrates the time evolution of these inter–base distances and the total purine path length (Total distance). Each system exhibits a distinct dynamic fingerprint. conf2 stands out as the most stable and compact structure: its total purine path length oscillates within a narrow band around ~55 Å throughout the simulation. However, the i_{67} distance in the central region where the ligand resides displays more pronounced and transient fluctuations, suggesting local "breathing" motions without compromising overall helical integrity. conf1 and conf3 are characterized by preferential instabilities at the termini. In conf1, the i_{12} distance remains stable for the first ~35 ns but undergoes a persistent disruption thereafter, settling in the 15–20 Å range. In conf3, a similar instability is observed at the opposite terminus (i_{1112}), manifesting as recurrent transient excursions up to ~15–20 Å. conf13 is the most dynamic and structurally heterogeneous system, where simultaneous large-amplitude fluctuations at both termini (i_{12} and i_{1112}) cause the total purine path length to vary over a wide range (~60–80 Å).

This time-resolved analysis provides a mechanistic basis for the statistical distributions in Fig. 30. The narrow distribution of conf2 reflects its overall structural integrity with localized central flexibility, whereas the intermediate variability of conf1 and conf3 arises from unilateral terminal disruptions. The broad, right-shifted distribution of conf13 reflects the cumulative effect of continuous bilateral perturbations induced by the two terminal ligands.

3.8.1. *Binding free energy analysis and energy decomposition (MM/GBSA)*

To establish a quantitative relationship between ligand binding affinity and the modulation of electronic conductance in DNA, a binding

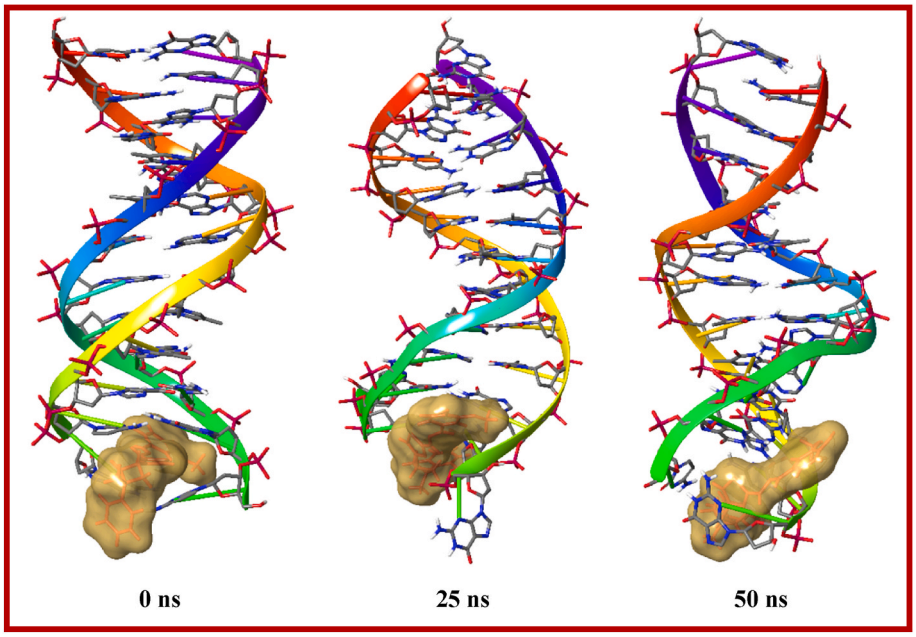

Fig. 28. Snapshots of conf3 system at 0, 25, and 50 ns, showing conformational changes and ligand stabilization within the major groove during the simulation.

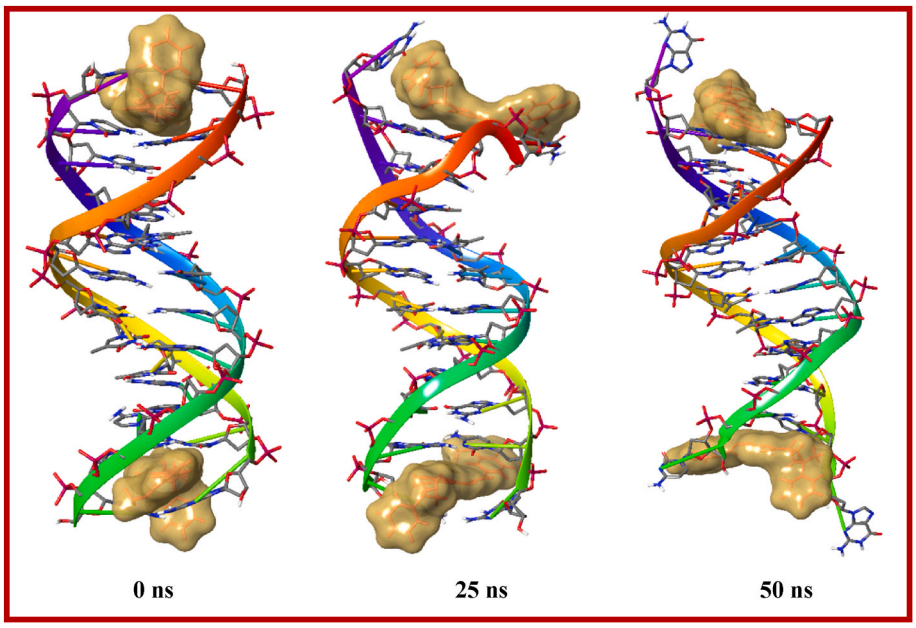

Fig. 29. Snapshots of conf13 system at 0, 25, and 50 ns, showing conformational changes and ligand stabilization within the major groove during the simulation.

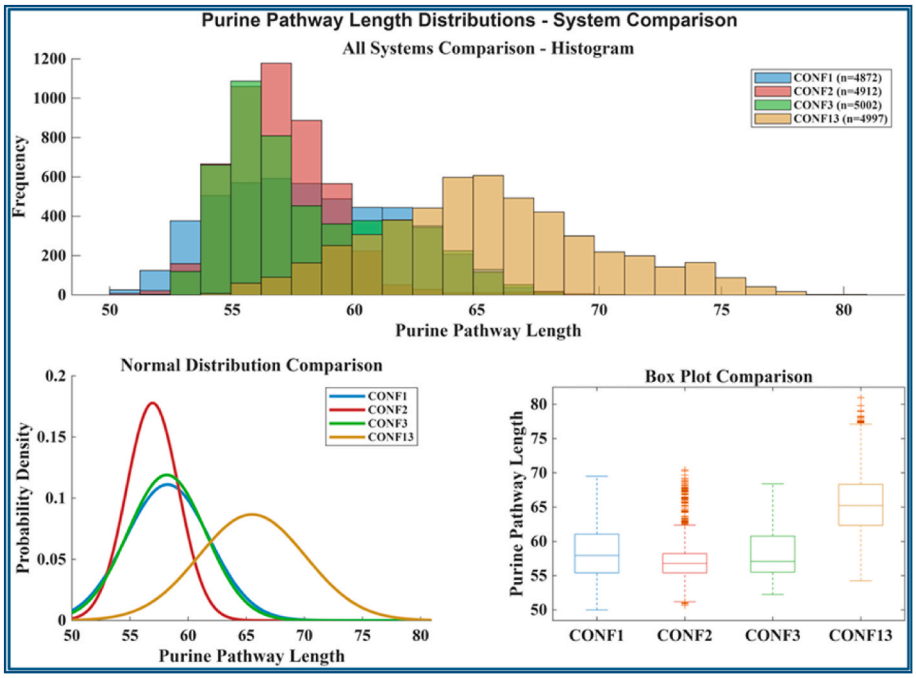

Fig. 30. Distribution of purine pathway lengths for conf1, conf2, conf3, and conf13. conf2 shows the most compact distribution, conf1 and conf3 exhibit intermediate variability, and conf13 displays a broadened right–shifted profile extending up to ~80 Å.

free energy analysis was performed for the four DNA–ligand complexes. This analysis, employing the Molecular Mechanics/Generalized Born Surface Area (MM/GBSA) method, not only determines the thermodynamic favorability of the binding event but also elucidates the key energetic components that drive or oppose the association.

The results reveal fundamental trends common to all systems. The primary driving forces for binding are van der Waals (ΔVDWAALS) and electrostatic (ΔEEL) interactions. Conversely, the polar solvation energy (ΔEGB; GB term) strongly opposes binding in all configurations, whereas the non–polar solvation contribution (ΔESURF) plays a minor but favorable role.

Table 4 summarizes the main energy components and the final binding free energies for the four configurations. At the enthalpic level (ΔTOTAL), the strongest binding is observed in the conf13 system (dual–terminal binding), with a ΔTOTAL of −30.13 kcal/mol. This is followed by conf2 (ΔTOTAL = −19.57 kcal/mol), conf3 (ΔTOTAL = −16.37 kcal/mol), and conf1 (ΔTOTAL = −15.80 kcal/mol). This trend is primarily attributed to the significantly more dominant van der Waals interactions in conf13 (ΔVDWAALS = −55.04 kcal/mol) compared to the other systems.

However, the final determinant of thermodynamic stability, ΔG_{bind}, incorporates the entropic penalty (−TΔS) in addition to the enthalpic contributions. The calculations indicate that the entropic penalty is significant and positive for all systems, confirming that the reduction in

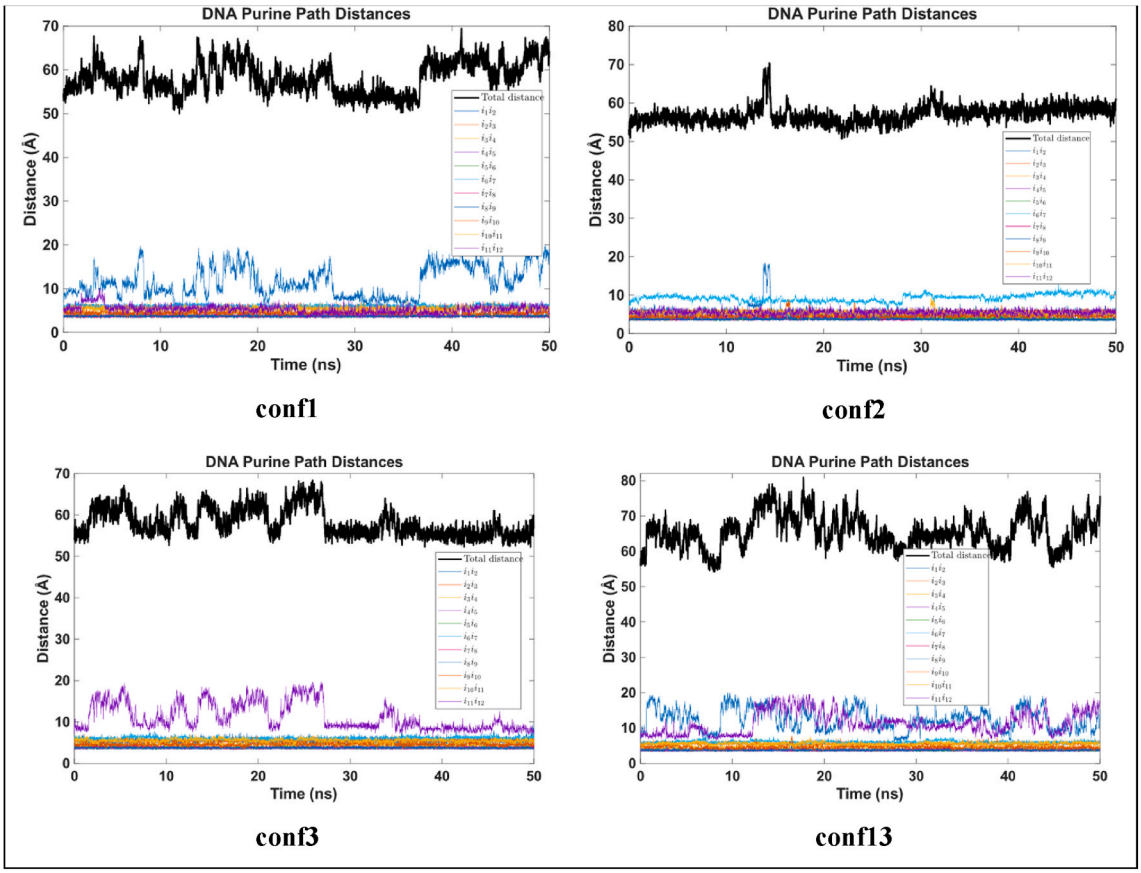

Fig. 31. Time evolution of purine path distances for the four systems (conf1, conf2, conf3, and conf13). In each panel, the total purine path length (black line) and the individual distances between adjacent purine bases along the path ($i_x i_y$, colored lines) are shown. The horizontal axis represents time (ns), and the vertical axis represents distance (Å).

Table 4
Summary of MM/GBSA energy components for the four DNA–ligand complexes. All values are in kcal/mol and were calculated using the Interaction Entropy (IE) method. The statistical uncertainties in the entropic contributions (see text) limit quantitative interpretation of the ΔG_{bind} values.

System	ΔVDWAALS	ΔEEL	ΔGSOLV	ΔTOTAL (ΔH)	–TΔS (IE)	ΔG_{bind} (IE)
conf1	−25.56	−13.63	23.39	−15.80	28.60	12.80
conf2	−37.37	−10.26	28.05	−19.57	16.50	−3.07
conf3	−29.34	−7.66	20.64	−16.37	26.13	9.77
conf13	−55.04	−19.18	44.10	−30.13	36.67	6.54

system disorder upon ligand binding is a thermodynamically unfavorable process. When entropic corrections are included, the nominal ΔG_{bind} values indicate that conf2 has the most favorable overall binding free energy, whereas conf1 and conf3 are less favorable and conf13 suffers from a particularly large entropic cost.

In interpreting these free energy values, however, the statistical uncertainty of the entropy term must be carefully considered. The standard deviation of the interaction energy, σ (Int. Energy), significantly exceeds the 3.6 kcal/mol threshold reported in the literature [48] (e.g., 8.38 kcal/mol for conf2 and 15.34 kcal/mol for conf13), which limits the quantitative accuracy of the interaction–entropy estimate and, consequently, of the final ΔG_{bind} values. In several cases, the associated uncertainty is comparable to, or larger than, the magnitude of ΔG_{bind} itself, so neither the sign of ΔG_{bind} nor the detailed quantitative ranking of the complexes can be regarded as statistically robust. For this reason, we use the MM/GBSA + IE analysis primarily to discern comparative stability patterns, where conf13 and conf2 exhibit the strongest enthalpic stabilization (most negative ΔTOTAL), conf1 and conf3 bind more weakly, and all complexes experience sizable entropic penalties that partly offset the enthalpic gain. Within these limitations, the data are consistent with the view that more strongly bound ligands (in the enthalpic sense) tend to induce stronger HOMO localization and greater conductance suppression, but they do not support a precise numerical binding–affinity ordering.

The pronounced differences in the dynamic stability of the complexes were further elucidated by examining the time–resolved binding free energy profiles (Figs. 32–35). The conf1 configuration represents the most dynamically stable binding mode, exhibiting the lowest standard deviation for its ΔTOTAL value (SD = 3.68 kcal/mol). In contrast, conf2, conf3, and notably conf13, displayed significantly higher standard deviations of 5.22 kcal/mol, 4.41 kcal/mol, and 6.44 kcal/mol, respectively. These broad fluctuations indicate the occurrence of transient instabilities or partial dissociation events throughout the simulation. conf13, which shows the largest fluctuation, stands out as the least dynamically stable complex. From a thermodynamic standpoint, the MM/GBSA results therefore identify conf2 as the configuration with the most favorable mean binding free energy ($\Delta G_{bind} \approx -3.1$ kcal/mol), whereas conf1, conf3, and conf13 display higher, weakly positive ΔG_{bind} values (Table 4). When this qualitative stability ranking is compared with the conductance data (Section 3.3, Table 2), it becomes evident that the most strongly bound complex (conf2) does not correspond to the highest conductance. Instead, conf3 – which is thermodynamically less favorable than conf2 – exhibits the largest G value among the ligand–-bound systems. This contrast indicates that, in the present DNA–ligand junctions, electronic transport is governed more by how the ligand perturbs the purine conduction pathway and localizes the HOMO than by the absolute magnitude of the binding free energy.

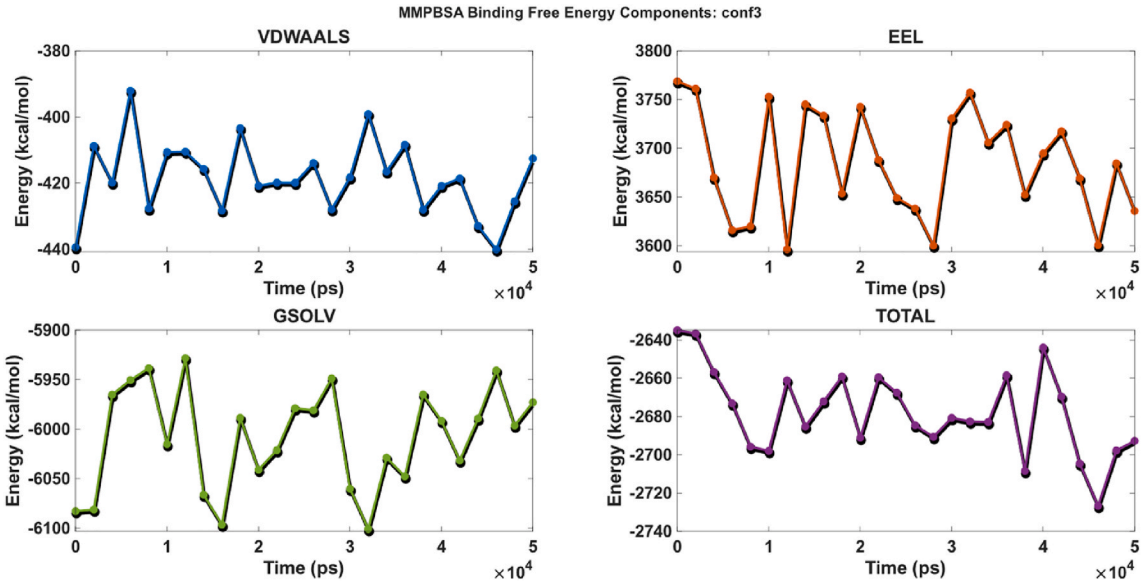

Fig. 32. Time evolution of binding free energy components (ΔVDWAALS, ΔEEL, ΔGSOLV, and ΔTOTAL) for the conf1 system over the 50 ns trajectory.

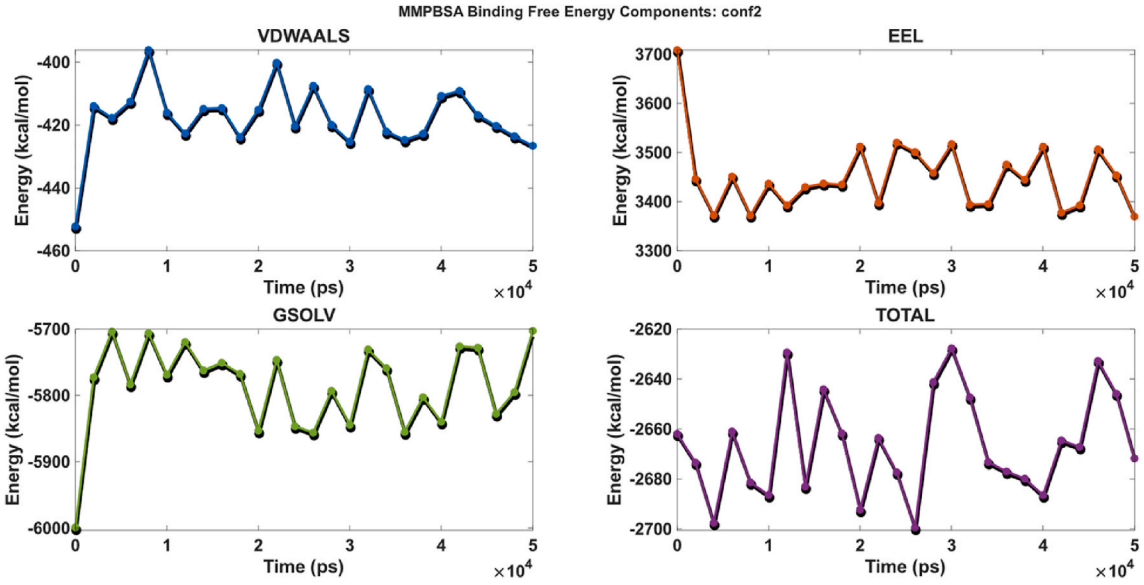

Fig. 33. Time evolution of binding free energy components (ΔVDWAALS, ΔEEL, ΔGSOLV, and ΔTOTAL) for the conf2 system over the 50 ns trajectory.

A component–wise decomposition quantitatively clarifies the origin of these dynamics. van der Waals (ΔVDWAALS) interactions provide the primary stabilizing force in all systems, with average values ranging from −25.56 kcal/mol (conf1) to −55.04 kcal/mol (conf13). In contrast, the electrostatic (ΔEEL) and polar solvation (ΔEGB) terms fluctuate dramatically and exhibit a strong anti–correlation. This is most evident in conf13, where the favorable ΔEEL of −19.18 kcal/mol is almost perfectly offset by the highly unfavorable ΔEGB penalty of +49.36 kcal/mol. The primary source of the large variability in ΔTOTAL is the high standard deviation of these terms (e.g., for conf13, SD(ΔEEL) = 12.48 kcal/mol and SD(ΔGSOLV) = 11.48 kcal/mol). Non–polar solvation (ΔESURF) contributes a small and stable stabilizing effect in all cases, ranging from −2.51 (conf1) to −5.26 kcal/mol (conf13).

Taken together, these findings suggest a qualitative hierarchy in binding behavior rather than a strictly quantitative free–energy ranking. conf2 and conf13 display the most pronounced van der Waals and electrostatic stabilization, consistent with their more extensive ligand–DNA contacts, whereas conf1 and conf3 show weaker enthalpic contributions. The interaction–entropy analysis further indicates that entropic penalties oppose binding in all cases and are particularly large for conf13, in line with its pronounced dynamic fluctuations. Thus, conf2 may be regarded as the configuration with the most favorable balance between enthalpic stabilization and entropic cost, while conf1, conf3, and conf13 represent less favorable compromises. However, given the sizeable statistical uncertainties discussed above, these trends should be interpreted as qualitative and not as definitive statements about absolute thermodynamic stability or the uniqueness of any single binding mode.

4. Conclusion

In this work, the electronic transport properties of the 12–base pair DNA duplex (102d) and its ligand–bound variants (conf1, conf2, conf3, and conf13) were systematically investigated using quantum transport calculations, molecular orbital analysis, DOS contour maps, transmission spectra, and conductance evaluations.

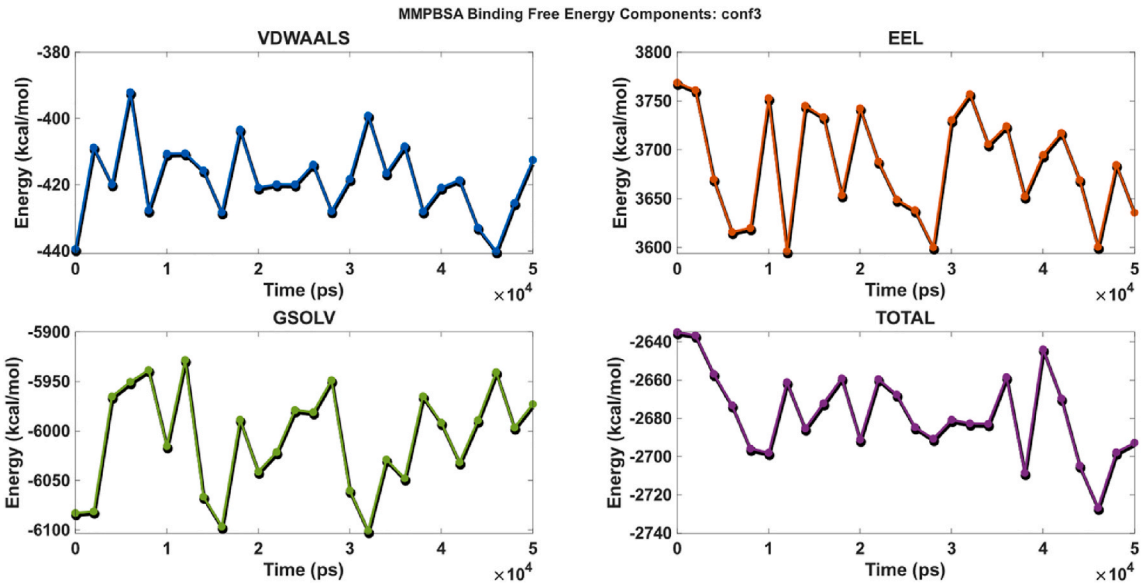

Fig. 34. Time evolution of binding free energy components (ΔVDWAALS, ΔEEL, ΔGSOLV, and ΔTOTAL) for the conf3 system over the 50 ns trajectory.

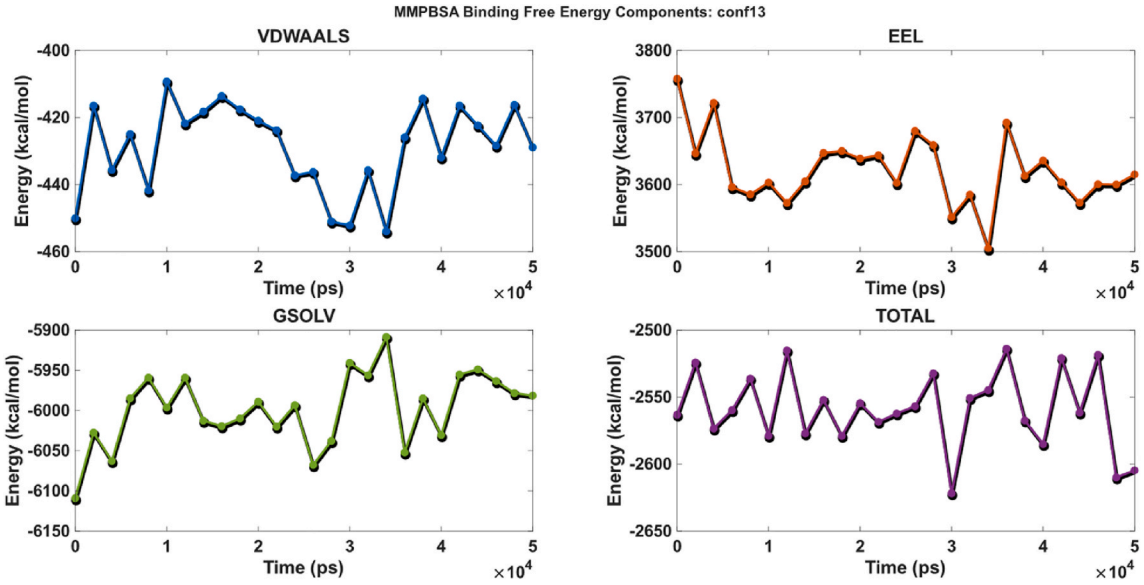

Fig. 35. Time evolution of binding free energy components (ΔVDWAALS, ΔEEL, ΔGSOLV, and ΔTOTAL) for the conf13 system over the 50 ns trajectory.

The pristine DNA duplex exhibited a wide band gap of 4.10 eV (HOMO at −5.07 eV, LUMO at −0.98 eV), consistent with its insulating nature. Its DOS contour maps revealed well–delocalized valence states across the DNA backbone, allowing limited but measurable charge transport. Upon ligand binding, however, the HOMO orbitals became strongly localized on the ligands, disrupting the delocalization along the DNA bases. This localization was confirmed by both contour map visualizations and numerical DOS values, showing that ligand contributions dominated over those of the neighboring base pairs.

Transmission and conductance analyses further highlighted the suppressive effect of ligands. The pristine duplex exhibited $G \approx 2.685 \times 10^{-4}$ G_0 at the HOMO level (Table 2). Relative to 102d, conductance decreased substantially in all ligand–bound systems: conf1 $= 6.340 \times 10^{-5}$ G_0 ($\Delta G = -76.39$ %), conf2 $= 7.002 \times 10^{-5}$ G_0 ($\Delta G = -73.92$ %), conf3 $= 8.874 \times 10^{-5}$ G_0 ($\Delta G = -66.95$ %), and conf13 $= 7.955 \times 10^{-5}$ G_0 ($\Delta G = -70.37$ %). Even when plotted on the relative ($E_F - E_{HOMO}$) scale, all systems exhibited a monotonic decay of conductance, indicating tunneling–dominated transport. Notably, conf13 (two terminal ligands) retained slightly higher conductance than conf1 and conf2, while conf3 displayed the highest conductance among the ligand–bound systems.

The binding free energy analysis, when considered together with the transport results, points to a complex relationship between thermodynamic stabilization and electronic perturbation. Because the statistical uncertainties associated with the MM/GBSA–IE calculations are comparable to the magnitudes of ΔG_{bind}, the resulting free-energy values cannot be used to establish a strict or unambiguous ranking of thermodynamic stability. Although the MM/GBSA–IE analysis yields nominally positive mean ΔG_{bind} values for conf1, conf3, and conf13, these values fall within the statistical uncertainty and likely reflect sizable entropic penalties that partially offset favorable enthalpic interactions; therefore, they should be interpreted as indicating marginal net stability on the MD timescale rather than definitive thermodynamic unfavorability. Nevertheless, the enthalpic components indicate that conf2 and conf13 are more strongly stabilized than conf1 and conf3, while all complexes experience sizable entropic penalties that partially offset this

stabilization. At the same time, the configuration with the highest conductance among the ligand-bound systems (conf3) does not coincide with the most favorable calculated binding energetics (conf2), and the lowest-conductance system (conf1) is not the weakest binder. Thus, our data do not support a simple one-to-one correlation between binding affinity and conductance suppression. Instead, they qualitatively highlight the dual role of ligands: they can enhance the thermodynamic stabilization of the duplex while modulating its long-range charge transport in a manner that depends sensitively on the binding mode and the associated orbital localization, rather than on binding strength alone.

Overall, the results demonstrate that while ligand intercalation effectively narrows the band gap of DNA, the induced orbital localization significantly reduces long–range charge transport. These findings highlight that the specific binding mode is as critical as the overall binding affinity (ΔG_{bind}) in determining the final electronic properties. This underlines the importance of considering not only frontier orbital energies but also their spatial distribution and the nuanced thermodynamic and structural consequences of binding when designing DNA–based molecular wires and nanodevices.

CRediT authorship contribution statement

Tuncay Karakurt: Writing – review & editing, Writing – original draft, Software, Resources, Project administration, Methodology, Investigation, Formal analysis, Data curation, Conceptualization. **Alaaddin Cukurovali:** Resources. **Hashem Mohammad:** Resources. **Ibrahim Yilmaz:** Resources.

Declaration of competing interest

The authors declare that they have no known competing financial interests or personal relationships that could have appeared to influence the work reported in this paper.

Acknowledgements

The numerical calculations reported in this paper were fully/partially performed at TUBITAK ULAKBIM, High Performance and Grid Computing Center (TRUBA resources).

Data availability

Data will be made available on request.

References

[1] R.G. Endres, D.L. Cox, R.R.P. Singh, Colloquium: the quest for high-conductance DNA, Rev. Mod. Phys. 76 (2004) 195–214.
[2] D. Porath, G. Cuniberti, R. Di Felice, Charge transport in DNA-based devices, Top. Curr. Chem. 237 (2004) 183–227.
[3] L. Xiang, J.L. Palma, Y. Li, V. Mujica, M.A. Ratner, N. Tao, Intermolecular quantum interference in DNA charge transport, Nat. Chem. 7 (2015) 221–226.
[4] H. Mohammad, M.P. Anantram, Charge transport through DNA with energy-dependent decoherence, Phys. Rev. E 108 (2023) 044403.
[5] L. He, L. She, L. Wang, C. Mi, K. Ma, M. Yu, C. Zhang, The electric regulation mechanism of drug molecules intercalating with DNA, Arch. Biochem. Biophys. 762 (2024) 110203.
[6] S.V. Aradhya, L. Venkataraman, Single-molecule electronics: from chemical design to technical devices, Nat. Nanotechnol. 8 (2013) 399–410.
[7] M. Alangari, B. Demir, C.A. Gultakti, E.E. Oren, J. Hihath, Mapping DNA conformations using single-molecule conductance measurements, Biomolecules 13 (2023) 129.
[8] L. Luo, S. Manda, Y. Park, B. Demir, J. Sanchez, M.P. Anantram, M. Rolandi, DNA nanopores as artificial membrane channels for bioprotonics, Nat. Commun. 14 (2023) 5364.
[9] Y. Li, J.M. Artés, B. Demir, S. Gokce, H.M. Mohammad, M. Alangari, J. Hihath, Detection and identification of genetic material via single-molecule conductance, Nat. Nanotechnol. 13 (2018) 1167–1173.
[10] J. Qi, N. Edirisinghe, M.G. Rabbani, M.P. Anantram, Unified model for conductance through DNA with the Landauer–Büttiker formalism, Phys. Rev. B 87 (2013) 085404.
[11] H. Mohammad, B. Demir, C. Akin, B. Luan, J. Hihath, E.E. Oren, M.P. Anantram, Role of intercalation in the electrical properties of nucleic acids for use in molecular electronics, Nanoscale Horiz. 6 (2021) 651–660.
[12] R. Gutierrez, Structural fluctuations and quantum transport through DNA molecular wires: a combined molecular dynamics and model Hamiltonian approach, New J. Phys. 12 (2010) 023022.
[13] H. Berney, J.M.D. Coey, C. Hassa, S. O'Reilly, Development, characterization and performance of DNA diagnostic biosensors, Sens. Actuators, B 68 (2000) 100–108.
[14] K. Sharma, N. Sehgal, A. Kumar, Biomolecules for development of biosensors and their application, Curr. Appl. Phys. 3 (2003) 307–316.
[15] H. Kargar, M. Fallah-Mehrjardi, M. Moghadam, H.R. Zare-Mehrjardi, A. Omidvar, N. Dege, E. Acar, M. Ashfaq, K.S. Munawar, M.N. Tahir, H.R. Shahsavari, Tricoordinate copper(I) complexes of N,N-bidentate schiff-base ligand: syntheses, crystal structure determinations, electrochemical properties, theoretical studies, and catalytic activities, Inorg. Chem. Commun. 182 (2025) 115512.
[16] H. Kargar, M. Fallah-Mehrjardi, M. Moghadam, A. Omidvar, H.R. Zare-Mehrjardi, N. Dege, M. Ashfaq, K.S. Munawar, M.N. Tahir, A novel iodo bridged 1D CuI coordination polymer containing N,N-bidentate Schiff base ligand: synthesis, structure, theoretical studies, electrochemical properties, and catalytic activity in the synthesis of tetrahydropyrimidines, Polyhedron 249 (2024) 116754.
[17] H. Kargar, M. Fallah-Mehrjardi, M. Moghadam, S. Yarahmadi, A. Omidvar, H. R. Zare-Mehrjardi, N. Dege, M. Ashfaq, K.S. Munawar, M.N. Tahir, H.R. Shahsavari, Structural and electrochemical properties of a Cu(I) schiff-base complex: catalytic application to the synthesis of tetrahydropyrimidine derivatives, Inorg. Chim. Acta. 570 (2024) 122160.
[18] H. Kargar, E. Parisi, M. Fallah-Mehrjardi, R. Centore, E. Santagata, P.P. Mazzeo, F. Abyar, A. Omidvar, K.S. Munawar, Experimental and theoretical studies of isoniazid hydrazone Schiff base ligands: synthesis, single crystal X-ray diffraction, spectral characterization, DFT, and molecular docking calculations, J. Mol. Struct. 1348 (2025) 143515.
[19] H. Kargar, M. Fallah-Mehrjardi, F. Abyar, A. Omidvar, N. Dege, M. Ashfaq, K. S. Munawar, M.N. Tahir, Coordination polymer of CuI incorporating a bidentate Schiff base ligand: synthesis, SC-XRD, HSA, DFT calculations, and molecular docking studies, J. Mol. Struct. 1349 (2025) 143758.
[20] A.X.S. Bruker, APEX (CCD Diffractometer) Software/Hardware, Bruker AXS Inc., Madison, WI, 2008.
[21] G.M. Sheldrick, SHELXT – integrated space-group and crystal-structure determination, Acta Crystallogr., Sect. A 71 (2015) 3–8.
[22] G.M. Sheldrick, Crystal structure refinement with SHELXL, Acta Crystallogr. C 71 (2015) 3–8.
[23] O.V. Dolomanov, L.J. Bourhis, R.J. Gildea, J.A.K. Howard, H. Puschmann, OLEX2: a complete structure solution, refinement and analysis program, J. Appl. Crystallogr. 42 (2009) 339–341.
[24] T.D. Kühne, M. Iannuzzi, M. Del Ben, V.V. Rybkin, et al., CP2K: an electronic structure and molecular dynamics software package – quickstep, J. Chem. Phys. 152 (2020) 194103.
[25] M.J. Abraham, T. Murtola, R. Schulz, S. Páll, J.C. Smith, B. Hess, E. Lindahl, GROMACS: high performance molecular simulations through multi-level parallelism from laptops to supercomputers, SoftwareX 1–2 (2015) 19–25.
[26] M.S. Valdés-Tresanco, M.E. Valdés-Tresanco, P.A. Valiente, E. Moreno, Gmx_MMPBSA: a new tool to perform end-state free energy calculations with GROMACS, J. Chem. Theor. Comput. 17 (2021) 6281–6291.
[27] M.J. Frisch, G.W. Trucks, H.B. Schlegel, et al., Gaussian 09, Revision A.1, Gaussian, Inc., Wallingford, CT, 2009.
[28] A.D. Becke, Density-functional thermochemistry. III. The role of exact exchange, J. Chem. Phys. 98 (1993) 5648–5652.
[29] C. Lee, W. Yang, R.G. Parr, Development of the Colle-Salvetti correlation-energy formula into a functional of the electron density, Phys. Rev. B 37 (1988) 785–789.
[30] W.J. Hehre, R. Ditchfield, J.A. Pople, Self-consistent molecular orbital methods. XII. Further extensions of gaussian-type basis sets, J. Chem. Phys. 56 (1972) 2257–2261.
[31] N. Russo, M. Toscano, A. Grand, Theoretical determination of electron affinity and ionization potential of DNA and RNA bases, J. Comput. Chem. 21 (2000) 1243–1250.
[32] E. Cauët, M. Valiev, J.H. Weare, Vertical ionization potentials of nucleobases in a fully solvated DNA environment, J. Phys. Chem. B 114 (2010) 5886–5894.
[33] J. Tomasi, B. Mennucci, R. Cammi, Quantum mechanical continuum solvation models, Chem. Rev. 105 (2005) 2999–3094.
[34] P.O. Löwdin, On the nonorthogonality problem, Adv. Quant. Chem. 5 (1970) 185–199.
[35] J.M. Artés, Y. Li, J. Qi, M.P. Anantram, J. Hihath, Conformational gating of DNA conductance, Nat. Commun. 6 (2015) 8870.
[36] K. Senthilkumar, F.C. Grozema, C.F. Guerra, F.M. Bickelhaupt, F.D. Lewis, Y. A. Berlin, M.A. Ratner, L.D.A. Siebbeles, Absolute rates of hole transfer in DNA, J. Am. Chem. Soc. 127 (2005) 14894–14903.
[37] S. Datta, Electronic Transport in Mesoscopic Systems, Cambridge University Press, Cambridge, 1995.
[38] R. Landauer, Spatial variation of currents and fields due to localized scatterers in metallic conduction, IBM J. Res. Dev. 1 (1957) 223–231.
[39] M. Büttiker, Coherent and sequential tunneling in series barriers, IBM J. Res. Dev. 32 (1988) 63–73.
[40] J.L. D'Amato, H.M. Pastawski, Conductance of a disordered linear chain including inelastic scattering events, Phys. Rev. B 41 (1990) 7411–7420.
[41] C.J.O. Verzijl, J.S. Seldenthuis, J.M. Thijssen, Applicability of the wide-band limit in DFT-based molecular transport calculations, J. Chem. Phys. 138 (2013) 094102.

[42] G. Horowitz, Validity of the concept of band edge in organic semiconductors, J. Appl. Phys. 118 (2015) 115502.
[43] W.W. Parson, Temperature dependence of the rate of intramolecular electron transfer, J. Phys. Chem. B 122 (2018) 8824–8833.
[44] F. Zahid, M. Paulsson, S. Datta, Electrical conduction through molecules, in: Advanced Semiconductor and Organic Nano-Techniques, Elsevier, Amsterdam, 2003, pp. 1–41.
[45] J. Olofsson, S. Larsson, Electron hole transport in DNA, J. Phys. Chem. B 105 (2001) 10398–10406.
[46] B. Giese, Long-distance electron transfer through DNA, Annu. Rev. Biochem. 71 (2002) 51–70.
[47] D. Porath, G. Cuniberti, R. Di Felice, Charge transport in DNA-based devices, Top. Curr. Chem. 237 (2004) 183–227.
[48] J. Jortner, M. Bixon, T. Langenbacher, M.E. Michel-Beyerle, Charge transfer and transport in DNA, Proc. Natl. Acad. Sci. U. S. A. 95 (1998) 12759–12765.
[49] V. Coropceanu, J. Cornil, D.A. da Silva Filho, Y. Olivier, R. Silbey, J.L. Brédas, Charge transport in organic semiconductors, Chem. Rev. 107 (2007) 926–952.
[50] A. Nitzan, M.A. Ratner, Electron transport in molecular wire junctions, Science 300 (2003) 1384–1389.
[51] R. Kumari, R. Kumar, A. Lynn, Open Source Drug discovery consortium, g_mmpbsa—A GROMACS tool for high-throughput MM-PBSA calculations, J. Chem. Inf. Model. 54 (2014) 1951–1962.
[52] C. Wang, D. Greene, L. Xiao, R. Qi, R. Luo, Recent developments and applications of the MMPBSA method, Front. Mol. Biosci. 4 (2018) 87.
[53] T. Hou, J. Wang, Y. Li, W. Wang, Assessing the performance of the MM/PBSA and MM/GBSA methods, J. Chem. Inf. Model. 51 (2011) 69–82.
[54] V. Ekberg, U. Ryde, On the use of interaction entropy and related methods to estimate binding entropies, J. Chem. Theor. Comput. 17 (2021) 5379–5391.